Journal of
Materials Chemistry C

ROYAL SOCIETY
OF CHEMISTRY

REVIEW

View Article Online
View Journal | View Issue

Check for updates

Cite this: *J. Mater. Chem. C*, 2024, **12**, 1609

Advances in the optical and electronic properties and applications of bismuth-based semiconductor materials

Peng Xia,†[ab] Yuan-Jun Song,†[ab] Yu-Ze Liu,[a] Mei-Xuan Long,[a] Cheng Yang,[a] Xiao-Yang Zhang[ab] and Tong Zhang *[abc]

Received 13th September 2023,
Accepted 18th December 2023

DOI: 10.1039/d3tc03329e

rsc.li/materials-c

In recent years, bismuth-based semiconductors have become a research hotspot in the new semiconductor field due to their unique optical and electronic properties. In addition, due to the simple fabrication process and controllable shape and size of these materials, they are widely used in the fields of optoelectronic devices, electrocatalysis, photocatalysis, biomedicine, *etc.* However, the current review papers on bismuth-based semiconductors mainly focus on the field of photocatalysis, while the applications of other fields are rarely reported, and the comprehensive summary of optical and electronic properties and applications of bismuth-based semiconductors are also lacking. Therefore, in this review, a variety of typical bismuth-based semiconductor materials are introduced in detail, including their lattice structures, optical and electronic properties and modification studies. In addition, the relationship between the bulk composition and photoelectric properties is analyzed, which will promote the future research on how to systematically control the photoelectric properties of bismuth-based materials. Secondly, the preparation methods of different bismuth-based semiconductor materials and applications in the field of optoelectronics are evaluated. Finally, the challenges faced by bismuth-based semiconductor materials in academic studies and industrial applications are pointed out, and the future work is prospected.

1. Introduction

Traditional semiconductor materials such as silicon, germanium, and gallium nitride have ignited an information technology revolution in integrated circuits and digital communications, profoundly impacting human society and economic development.[1] However, these conventional semiconductors face issues such as low photoelectric conversion efficiency, susceptibility to thermal damage, high production costs, and environmental pollution, inhibiting their applications in emerging fields like new energy, environmental protection and biomedicine.[2,3] To address these limitations, much efforts have been exerted on exploring various new semiconductor materials, such as InSe,[4] TiO_2,[5] and Ga_2O_3.[6] Nonetheless, these alternatives also have inherent drawbacks that hinder their applications in optoelectronics. For example, two-dimensional semiconductor materials often exhibit unstable lattice structures[7] and organic semiconductors suffer from low crystallinity, making it challenging to control their morphologies and sizes.[8] In addition, perovskite materials with excessively large band gaps result in poor visible light absorption.[9] In contrast, bismuth-based semiconductors offer several advantages, including facile synthesis, affordability, environmental compatibility, high stability, and exceptional visible light activity; therefore, they are gaining much more attention in the fields of photocatalysis, solar cells, and photoelectrochemistry.[10–13] Especially in the field of photocatalysis, bismuth-based semiconductors have been demonstrated to exhibit promising photocatalytic performance in many reactions (such as CO_2 reduction, degradation of organic pollutants) under visible light because of their unique electronic and optical properties.[14,15] In comparison to typical photocatalysts, these bismuth-based materials show appropriate band gaps or a wide range of visible light response which can promote the absorption of visible light and separation of photogenerated electron–hole pairs, ultimately leading to enhanced photocatalytic efficiency.[16,17] Besides, some bismuth-based semiconductor photocatalysts with unique hierarchical porous structures can increase the diffusion of reactants and provide additional

---

[a] *School of Electronic Science and Engineering, Southeast University, Nanjing 210096, China. E-mail: tzhang@seu.edu.cn*

[b] *Suzhou Key Laboratory of Metal Nano-Optoelectronic Technology, Suzhou Research Institute of Southeast University, Suzhou 215123, China*

[c] *Key Laboratory of Micro-Inertial Instrument and Advanced Navigation Technology, Ministry of Education, and School of Instrument Science and Engineering, Southeast University, Nanjing 210096, China*

† These authors contributed equally.

reaction sites, resulting in improved photocatalytic performance. On the other hand, for those typical photocatalysts, due to either an inappropriate band gap or insufficient response to visible light, they often encounter low photocatalytic activity or selectivity of desirable product problems. For example, TiO_2 as one of the most commonly utilized photocatalysts is predominantly active in the ultraviolet light range since its wide band gap restricts its practical applications under solar light. Although several modification methods through doping have been employed on TiO_2 to enhance its visible light absorption, doped materials are introduced as recombination centres leading to decreased photocatalytic activity.[18] In addition, recently, CdS, WO_3, and $AgVO_3$ have also been hotspots in photocatalytic research due to their narrow band gaps and strong absorption in the visible light region. However, the rapid radiative recombination of photogenerated electrons and holes of CdS coupled with the high kinetic barrier for hydrogen evolution on surface hinders the direct conversion of solar energy to fuels.[19] Another example, WO_3 with a band gap ranging from 2.4 to 2.8 eV is also a notable candidate in visible-light-driven photocatalysis, while its lower conduction band level poses a limitation in the photocatalytic reduction potential of the electrons, resulting in a decrease in product selectivity and light-energy conversion efficiency.[20] Moreover, in the case of $AgVO_3$, the photogenerated electrons tend to reduce Ag^+ to Ag nanoparticles which introduces a photo-corrosion risk for silver-based catalysts.[21] Hence, bismuth-based photocatalysts with appropriate band gaps, visible light response, high stability, resistance to photocorrosion, and tunable and controllable electronic and optical properties are explored.

Although the community is continuing to conduct extensive investigations into physical and chemical properties of bismuth-based semiconductors, their synthesis methodologies and applications, numerous opportunities and challenges still need further breakthroughs, especially the in-depth study on how to control their morphology and crystal structures and optimize optical and electronic properties. In addition, these published review papers on bismuth-based semiconductors mainly concentrate on the area of photocatalysis and there is a lack of complete picture of the recent advances in the optical and electronic properties and applications of bismuth-based semiconductors, as well as the latest developments and breakthroughs in this field.[16–18,22–36] Therefore, this review will focus on comprehensive introduction and analysis of these aspects. As shown in Fig. 1, firstly, we will give discussions of distinctive characteristics of various types of bismuth-based semiconductors, including their unique crystal structures and electronic structures. Then the commonly utilized synthesis techniques for bismuth-based semiconductor materials will be outlined with the analysis of effect of material morphology on the photoelectronic properties. Additionally, applications of bismuth-based semiconductors in different fields such as optoelectronic devices, electrocatalysis, photocatalysis, and medical applications will be presented. Lastly, the article provides a summary of the prevailing research challenges associated with bismuth-based semiconductors in terms of their properties, synthesis methodologies, practical applications as well as prospects.

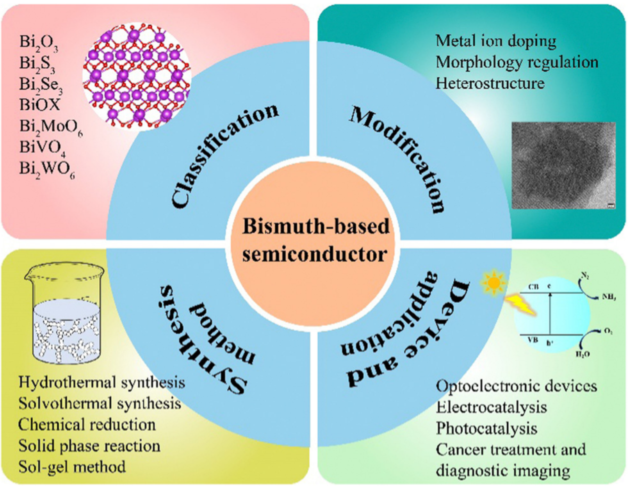

Fig. 1 The schematic diagram outlining the main content of this review.

2. Classification of bismuth-based semiconductors

2.1. Bismuth oxide

Bismuth trioxide (Bi_2O_3) as the simplest and most pivotal type of bismuth-based compounds (Fig. 2(a)),[17,37] shows a relatively narrow band gap (ranging from 2.2 to 2.8 eV, see Fig. 3(a)) and a robust capacity for deep valence band oxidation, positioning it as a potential photocatalyst under visible light. Furthermore, the cost-effective preparation, commendable oxygen ion conductivity, chemical and biological inertness, resistance to photo-corrosion, and its ability to absorb visible light all contribute to making Bi_2O_3 a promising optoelectronic material for

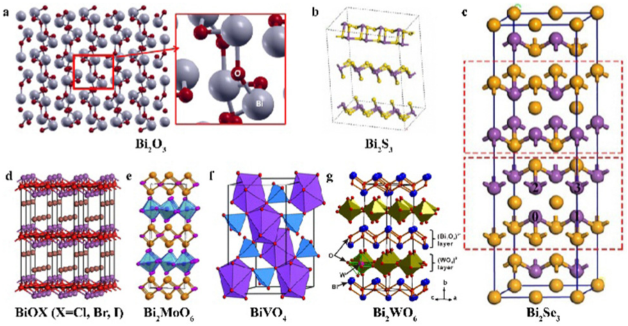

Fig. 2 The crystal structures of (a) Bi_2O_3, reproduced from ref. 37 with permission from Elsevier, copyright 2017. (b) Bi_2S_3, reproduced from ref. 55 with permission from Elsevier, copyright 2022. (c) Bi_2Se_3, reproduced from ref. 66 with permission from Elsevier, copyright 2023. (d) BiOX (X = Cl, Br, I), reprinted with permission from ref. 73. Copyright 2014 American Chemical Society. (e) Bi_2MoO_6, reproduced from ref. 93 with permission from Elsevier, copyright 2014. (f) $BiVO_4$, reproduced from ref. 107 with permission from Royal Society of Chemistry, copyright 2011. (g) Bi_2WO_6, reproduced from ref. 119 with permission from Springer Nature, copyright 2020.

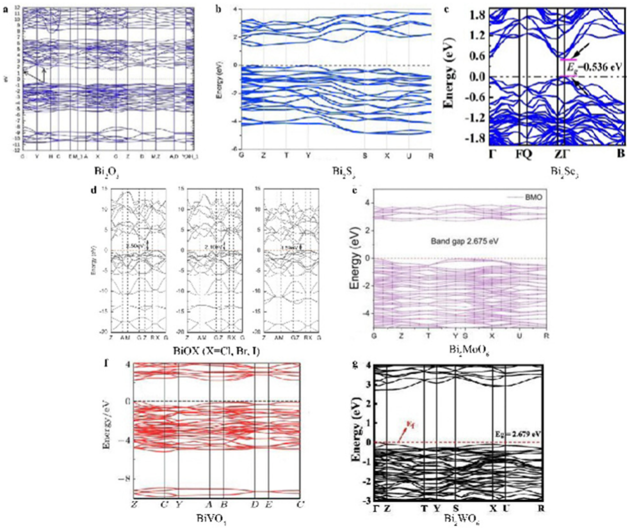

Fig. 3 The energy band structures of (a) Bi_2O_3, reproduced from ref. 37 with permission from Elsevier, copyright 2017. (b) Bi_2S_3, reproduced from ref. 54 with permission from Elsevier, copyright 2020. (c) Bi_2Se_3, reproduced from ref. 66 with permission from Elsevier, copyright 2023. (d) BiOX (X = Cl, Br, I), reproduced from ref. 78 with permission from Elsevier, copyright 2012. (e) Bi_2MoO_6, reproduced from ref. 95 with permission from Elsevier, copyright 2022. (f) $BiVO_4$, reproduced from ref. 106 with permission from IOP Publishing Ltd, copyright 2017. (g) Bi_2WO_6, reproduced from ref. 117 with permission from Elsevier, copyright 2022.

environmental and energy-related applications.[38] For example, Zhang's group has demonstrated the ability of Bi_2O_3 nanoparticles to generate highly functional free radicals under exposure to visible light, which enables oxidative degradation of organic pollutants when they are adsorbed on the surface of these nanoparticles.[39] Other researchers also have reported that Bi_2O_3 can degrade various substances such as rhodamine B (RhB), methyl orange (MO), methylene blue, dichlorophenol, textile printing and dyeing wastewater, nitrite-containing wastewater, and volatile organic pollutants.[40–47]

However, because of its inherent material properties, Bi_2O_3 shows ready electron–hole recombination[48] and unstable crystal phases,[17] which significantly limits its optoelectronic applications and development. In particular, the chemical instability of Bi_2O_3 readily causes an α to δ phase transition during heating reactions, and even further to $(BiO)_2CO_3$, significantly deactivating relative performances. To address these problems, researchers have modified Bi_2O_3 through approaches like metal ion doping, morphology control, and heterostructure construction to enhance photoelectric performance.[49–53] For example, Nd-doped Nd/Bi_2O_3 nanocomposites can change original band structure of Bi_2O_3 and inhibit internal electron–hole recombination, leading to improved photocatalytic activity, excellent catalytic stability and reproducibility for hydrogen production.[49] Moreover, flower-like Bi_2O_3/TiO_2 made by Zhu's group enriched with Bi_2O_3 quantum dots on the surface enhances light absorption, photosensitivity, and hydrothermal stability due to its special morphology, which results in stronger photocatalytic activity and stability.[50] Additionally, heterostructures like Bi_2O_3/BiOCl,[51] Bi_2O_3/Bi_2SiO_5[52] and Bi_2O_3/PbS[53] have also been reported which exhibit higher charge separation and transfer efficiency, improved photocatalytic activity, and enhanced photoelectrochemical performance.

2.2. Bismuth chalcogenide

Bismuth sulfide (Bi_2S_3) is a typical transition metal sulfide semiconductor (Fig. 2(b)) with a wide visible light response range (absorption coefficient of 10^4–10^5 cm^{-1} and around 5% photoelectric conversion rate), high biocompatibility, and low toxicity. Additionally, Bi_2S_3 shows a narrow and variable band gap (1.3–1.7 eV, see Fig. 3(b)) depending on its morphology (nanoplates, nanorods, nanowires, *etc.*).[12,54,55] Bao *et al.* synthesized Bi_2S_3 nanowire arrays hydrothermally, exhibiting nonlinear current–voltage characteristics and good light response.[56] Later, Hu *et al.* assembled flower-like Bi_2S_3 nanorods and achieved controlled synthesis of monodispersed nanorods with excellent electrochemical hydrogen storage.[57] Bi_2S_3 nanorods produced by Zhou's group can enable sensitive detection of DNA methylation in novel PEC biosensors.[58] Thus, Bi_2S_3 shows great potential for application in solar cells, hydrogen storage, photocatalysis, optical detection, and memristors.[59] However, the narrow band gap of Bi_2S_3 leads to fast electron–hole recombination, reducing response speed and photocatalytic efficiency.[12] To suppress recombination, approaches like element doping,[60] conductive material modification,[61] and heterojunction structures[62–65] have been investigated. For example, modified $SrTiO_3$/Bi_2S_3 heterojunctions exhibit lower carrier recombination and electron transfer resistance than pure $SrTiO_3$ and Bi_2S_3, promoting UV-driven hydrogen production by effectively separating photogenerated carriers.[62] Combining Bi_2S_3 with the other wide-bandgap photocatalysts like TiO_2,[63,64] Bi_2WO_6,[64] and CdS[65] can also reduce electron–hole recombination and enhance visible light photocatalytic performance.

Bismuth selenide (Bi_2Se_3), another noteworthy bismuth chalcogenide, has been recognized for its remarkable characteristics as a visible-light-responsive semiconductor. As shown in Fig. 2(c) and 3(c), the layered structure, coupled with a narrow band gap ranging from 0.35 to 1.2 eV, makes it attractive for the photocatalytic degradation of organic pollutants.[23,66] Additionally, Bi_2Se_3 exhibits an insulating bulk state and massless Dirac surface states, contributing to its unique optical and electrical properties. The nanostructure of Bi_2Se_3 enhances surface state properties, particularly its metallic surface states with a zero band gap, facilitating the presence of a substantial number of itinerant electrons on its surface—a feature advantageous for photocatalytic reactions.[67,68] For instance, Lei *et al.* demonstrated enhanced photodegradative activity by preparing Bi_2Se_3-deposited TiO_2 nanobelts, surpassing the performance of pure TiO_2. This improvement was attributed to the quantum size effect of Bi_2Se_3.[69] Furthermore, to address the poor redox capacity and rapid carrier recombination of Bi_2Se_3, a Bi_2Se_3/g-C_3N_4 composite photocatalyst with an S-scheme configuration was prepared to enhance charge separation. This configuration resulted in a higher photocatalytic activity compared to pristine Bi_2Se_3 and g-C_3N_4 in the removal of phenol.[68] In summary, the outstanding light absorption, metallic surface, and high conduction-band properties of Bi_2Se_3 are attributed to the growing attention in the field of photocatalysis,[68,69] infrared detection,[70] and electrocatalysis.[71]

2.3. Bismuth-based oxyhalides

BiOX (X = Cl, Br, I) belongs to the V–VI–VIII ternary semiconductor group and has an orthorhombic structure (space group *P4/nmm*) like PbFCl (see Fig. 2(d)).[72,73] The BiOX crystal layered structure contains $[Bi_2O_2]^{2+}$ layers and double X atom layers stacked along the *C*-axis, connected through van der Waals interactions,[74] which generates an internal electrostatic field along the [001] direction, facilitating photogenerated charge migration within the crystal and leading to enhanced photocatalytic activity and photoconductivity.[75] Due to these excellent photoelectric properties, unique layered structure, good photocatalytic activity, and stability, BiOX materials have attracted much academic community interest.[76]

To deeply study photoelectric properties and applications of BiOX, the band structure and photo-response have been systematically investigated using density functional theory (DFT). DFT calculations (see Fig. 3(d)) show an interesting decrease of the band gap as the atomic number of X increases from Cl to I (2.50, 2.10 and 1.59 eV for BiOCl, BiOBr, and BiOI, respectively) which is related to their photocatalytic activity.[77,78] The wide band gap of BiOCl provides excellent photocatalytic activity solely under UV irradiation, while the narrowest band gap of BiOI enables visible and near-infrared activation but with relatively weak photocatalytic activity due to high electron–hole recombination. In contrast, BiOBr with moderate band gap shows potential as a visible light-responsive catalyst for solar energy conversion.[79] DFT results also indicate BiOX (X = Cl, Br, I) with an indirect band gap where photogenerated electrons must transit through intermediate k-layers before recombining with valence band holes can reduce electron–hole recombination rates.[80]

In summary, the unique layered structure and indirect band gap of BiOX enable high charge transfer rates and low carrier recombination, which promotes excellent performance for organic pollutant degradation,[81,82] alcohol oxidation,[82] and water splitting.[79] For example, it has been demonstrated that BiOCl can elevate photocatalytic Hg^0 oxidation under UV irradiation,[83] while BiOBr can drive degradation of ciprofloxacin (CIP) under visible light.[81] Like BiOX, bismuth-rich oxyhalides $Bi_xO_yX_z$ (*e.g.* Bi_3O_4Cl, $Bi_4O_5Br_2$, Bi_5O_7I) also possess layered structures with weak interlayer interactions, attracting increasing attention for their unique photoelectric properties.[84] $Bi_4O_5Br_2$, for instance, degrades ciprofloxacin at 91% in 150 minutes, around 1.5 times faster than BiOBr, while extending visible light absorption from 440 nm to 500 nm.[85]

2.4. Bismuth-based metal oxides

2.4.1. Bismuth molybdate. Bismuth molybdate (Bi_2MoO_6) belongs to the Aurivillius oxide family, with the general formula $Bi_2O_3{\cdot}nMoO_3$.[14] When *n* equals 3, 2, and 1, it corresponds to three phases: α-$Bi_2MO_3O_{12}$, β-$Bi_2MO_2O_9$, and γ-Bi_2MoO_6. For α-$Bi_2MO_3O_{12}$ and β-$Bi_2MO_2O_9$, the presence of defects and abundant active sites makes them effective catalysts for reactions like propylene oxidation to acrolein[86,87] and 1-butene conversion to butadiene and 2-butene.[88] On the other hand, γ-Bi_2MoO_6 possesses a layered structure,[89] with $[Bi_2O_2]^{2+}$ layers alternating with MoO_6 perovskite layers,[90] exhibiting excellent visible light absorption and charge separation (see Fig. 2(e)).[91–93] This unique property has been confirmed in the DFT study by Lai's group that γ-Bi_2MoO_6 is a direct band gap (2.5–2.8 eV, see Fig. 3(e)) semiconductor and enables visible light response.[94,95] In addition, people found that γ-Bi_2MoO_6 can be applied to many applications like organic degradation,[96] water splitting,[97] and CO_2 reduction.[98] For example, Bi_2MoO_6 can catalyse visible light-driven phenol degradation,[96] but suffers from fast carrier recombination and insufficient visible light absorption.[89] To address this problem, Li *et al.* synthesized mesoporous Bi_2MoO_6 spheres with increased specific surface area and charge transfer efficiency.[99] Additionally, Phuruangrat *et al.* claimed that tungsten-doped Bi_2MoO_6 boosted rhodamine B degradation rates by 1.69 times in comparison to Bi_2MoO_6.[100] Thus, approaches like morphology control,[99] metal doping,[101] and heterojunction structures[102] can effectively improve Bi_2MoO_6 photoelectric properties.

2.4.2. Bismuth vanadate. As an important bismuth-based oxide semiconductor, bismuth vanadate ($BiVO_4$) shows excellent visible light absorption, suitable band edge position, electrochemical stability, non-toxicity, and resistance to photochemical/chemical corrosion.[103,104] $BiVO_4$ has three crystal structures: tetragonal scheelite, monoclinic scheelite, and tetragonal zircon.[28] The monoclinic scheelite structure (m-$BiVO_4$, see Fig. 2(f)) exhibits the highest thermodynamic stability and catalytic activity, making it the most utilized photoelectrocatalyst.[103,105] Theoretical DFT calculations indicate that m-$BiVO_4$ is an indirect band gap semiconductor with a band gap of 2.4 eV, as illustrated in Fig. 3(f), which leads to full visible light absorption and utilization.[106] For m-$BiVO_4$, the conduction band is mainly derived from the V 3d orbitals, while the valence band arises from hybridized Bi 6s and O 2p orbitals.[104] Two distinct V–O bond lengths (1.77 Å and 1.69 Å) exist in m-$BiVO_4$, affected by Bi 6s/O 2p lone pair hybridization at the valence band maximum, causing distortions in the BiO_8 dodecahedra and VO_4 octahedra and displacing the positive and negative charge centres. Thus the resulting internal electric field promotes separation of photogenerated electrons and holes, enhancing the photoelectric properties of m-$BiVO_4$.[103,107] An earlier study by Kudo *et al.*[108] has shown that $BiVO_4$ exhibits broad-spectrum absorption under ultraviolet and visible light, causing high photocatalytic activity. Since then, significant studies have been carried out on the unique and excellent photoelectric properties of $BiVO_4$ and suggest a wide range of applications in fields such as organic pollutant degradation,[109] water splitting,[110] CO_2 reduction,[111] and photoanodes.[112] In order to further improve the photocatalytic activity, visible light absorption intensity, and other photoelectric properties of $BiVO_4$, researchers have also attempted to improve the high electron–hole recombination rate and poor electron mobility of

$BiVO_4$ by element doping,[113] vacancy introduction,[114] or heterostructure construction.[115] Furthermore, the low raw material cost and versatile preparation methods of $BiVO_4$, such as solid-phase reaction (SSR), high-temperature melting reaction, precipitation, and hydrothermal methods,[17] make it more promising and widely studied in the field of photocatalysis.

2.4.3. Bismuth tungstate. Bismuth tungstate (Bi_2WO_6) is another common bismuth-based oxide semiconductor with a perovskite layered structure, narrow band gap (2.8 eV, see Fig. 3(g)), strong visible light harvesting ability, non-toxicity, and high chemical stability.[116,117] Its crystal structure belongs to the orthorhombic space group *Pca*2(1)[17] and is formed by the superposition of $[Bi_2O_2]^{2+}$ and $[WO_4]^{2-}$ layers,[118,119] as depicted in Fig. 2(g). The layered structure of Bi_2WO_6 leads to sufficient adsorption sites and generates a built-in electric field between layers, which is beneficial to the separation of photogenerated electrons and holes.[120] According to the DFT calculation results, the valence band of Bi_2WO_6 is composed of the hybrid orbitals of Bi 6p and O 2p, while the conduction band is mainly contributed by the W 5d orbital, with the contribution of Bi 6p being small.[121] This kind of electronic structure brings about a broad dispersion of the valence bands, which increases the mobility of photogenerated holes and facilitates the oxidation reaction.[118]

As early as 1999, Akihiko *et al.* first synthesized Bi_2WO_6 *via* traditional solid-state reaction for photocatalytic O_2 generation.[122] After that, various methods like solid-state reaction, liquid-phase precipitation, hydrothermal methods, and solvothermal methods have been developed to produce Bi_2WO_6.[123] Currently, the application range of Bi_2WO_6 has covered organic pollutant degradation,[124] selective organic synthesis[125] and bacteria inactivation in aqueous solutions,[126] such as the photocatalytic degradation of rhodamine B/phenol mixtures[124] or *Escherichia coli* inactivation.[126] However, high photogenerated electron–hole recombination limits its photocatalytic performance. Strategies to address this include morphology control,[127] doping,[128] and heterojunction construction.[129] For instance, metal doping (Fe, Zn, and Mo) improves the visible light absorption and charge transfer of Bi_2WO_6.[128] Notably, the photocurrent density of Mo-doped Bi_2WO_6 is 57 times higher than that of pure Bi_2WO_6, dramatically enhancing the photoelectric properties.

3. Synthesis of bismuth-based materials

3.1. Hydrothermal method

Hydrothermal synthesis involves crystallization of single crystal materials from high-temperature aqueous solutions[130] and is commonly used to prepare bismuth-based compounds.[131] Compared to other methods, hydrothermally prepared nanoparticles often exhibit superior performance for targeted applications.[131] The process is energy-efficient and economical, yielding appropriately sized and shaped nanoparticles.[28] Moreover, effective control of product crystal phase, particle size, and morphology can be achieved by tuning parameters like solvent, temperature, time, pH, and reactant concentrations.[130] However, specialized autoclave reactors mean longer production times and lower efficiency than other methods.[132] Still, the hydrothermal synthesis method is important for bismuth-based single crystals and nanostructures since particles synthesized using this method show high crystallization and well-controlled morphology.

For example, tubular defective bismuth oxide (BiO_2) microtubes with a hierarchical hollow structure (see Fig. 4(a) and (b)) were first synthesized by Su *et al. via* hydrothermal synthesis,[133] which promotes efficient photogenerated electron–hole separation, enabling degradation of dyes like methyl orange and malachite green. Additionally, bismuth-based oxyhalides and metal oxides with controllable crystal facets and morphologies were prepared by using hydrothermal methods such that their optical properties can be systematically manipulated, which will be beneficial for specific applications in different fields. Zhang *et al.* selectively synthesized BiOCl {001} and {010} single crystal nanosheets using a 160 °C hydrothermal process.[134] In the case of {001}-exposed nanosheets, it exhibited higher ultraviolet pollutant degradation, while visible light favoured {010}-exposed nanosheets for dye degradation. Lin *et al.* hydrothermally synthesized monoclinic $BiVO_4$ with diverse morphologies like hollow spheres, decahedrons, coral-like particles, and needles (see Fig. 4(c)–(f)) by tuning pH and showed desirable

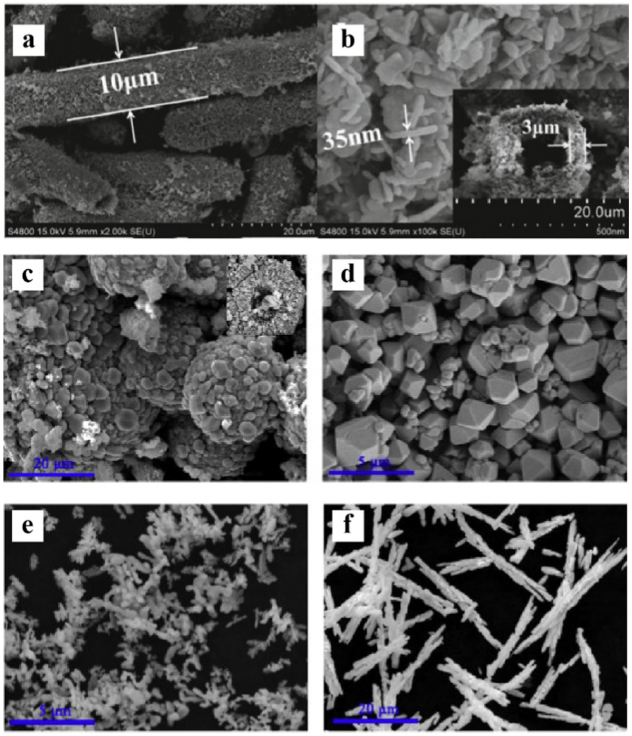

Fig. 4 (a) and (b) SEM images of the as-prepared BiO_2 microtubes. Reproduced from ref. 133 with permission from Elsevier, copyright 2018. SEM images of $BiVO_4$ powder prepared at different pH: (c) 0.5, (d) 2, (e) 7, and (f) 12. Reproduced from ref. 135 with permission from Elsevier, copyright 2019.

photocatalytic degradation efficiency toward rhodamine B solution.[135] Among them, $BiVO_4$ synthesized at pH 7 exhibited the best photocatalytic degradation efficiency under visible light, which demonstrates that pH can alter the $BiVO_4$ microstructure and photocatalytic performance. Furthermore, Zhang *et al.* tried microwave-assisted hydrothermal synthesis to shorten reaction times and reduce energy costs *vs.* traditional hydrothermal methods.[136] The resulting Bi_2CrO_6 crystals with exposed {001} planes and regular flake morphologies were demonstrated to exhibit enhanced photogenerated charge separation and photocatalytic hydrogen production owing to their high crystallinity and uniformity. However, hydrothermal method faces a challenge for the formation of low-dimensional materials (*e.g.*, 0D nanoparticles, 1D nanorods or nanoribbons, and 2D nanosheets).

3.2. Solvothermal method

The solvothermal method offers a solution to the challenge encountered in the hydrothermal method by applying organic solvents like polyols and citric acid instead of water to induce directional nucleus growth and nanoparticle assembly into 3D hierarchical structures. Mixed solvents of ethylene glycol with water, ethanol, or isopropanol can also increase anionic salt solubility and adjust ethylene glycol viscosity to improve product morphology and crystallinity.[137–139] As a result, solvothermal routes are more prevalent for preparing bismuth-based photocatalysts than the hydrothermal method.[131,140]

Solvothermal methods have been conducted to produce bismuth-based materials like metal-modified bismuth oxyhalides which exhibit unique electronic and optical properties. For example, Huang *et al.* successfully loaded Bi nanoparticles (~4.0 nm diameter) onto BiOBr nanoplates by reducing $Bi(NO_3)_3$ in ethylene glycol reductant *via* a solvothermal approach, as shown in Fig. 5(a)–(c).[141] The obtained Bi/BiOBr Schottky junction promotes interfacial electron transfer and nitrogen adsorption. Additionally, Chen *et al.* solvothermally synthesized Bi-modified $Bi_4O_5I_2$ microspheres in ethylene glycol (see Fig. 5(d)),[142] which generates a built-in electric field between Bi and $Bi_4O_5I_2$ that improves carrier separation efficiency. Owing to the synergistic effects of oxygen vacancies and this built-in field, the $Bi/Bi_4O_5I_2$ microspheres exhibit excellent mercury removal, performance stability, and sulfur resistance. However, like hydrothermal methods, solvothermal approaches still have long production cycles and lower yields. They also show the risks of harmful solvent emissions and environmental pollution.[143]

3.3. Chemical reduction method

Chemical reduction is another common synthesis method for bismuth-based nanomaterials. Similar to hydrothermal approaches, chemical reduction method is relatively inexpensive and can be operated under mild conditions (low temperature and pressure), enabling simple and green chemistry.[28,143] For example, Hamza *et al.* chemically synthesized $Bi_2(CrO_4)_3$ spherical nanoparticles with uniform size using a simple template-free and stabilizer-free chemical reduction at room temperature,[144] as depicted in Fig. 5(e). Photocatalytic tests revealed these spherical $Bi_2(CrO_4)_3$ nanoparticles can enhance hydrogen production activity in comparison to other reported Bi-based photocatalysts.

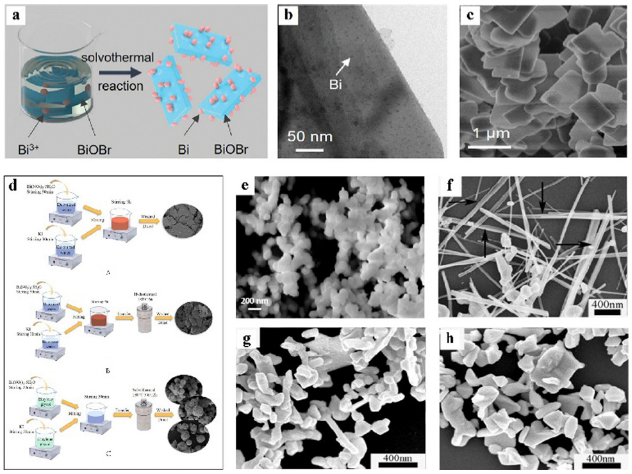

Fig. 5 (a) Schematics of the preparation of Bi/BiOBr composites. (b) TEM and (c) SEM image Bi/BiOBr. Reproduced from ref. 141 with permission from John Wiley and Sons, copyright 2021. (d) The preparation process of BiOI, $Bi_4O_5I_2$ and $Bi/Bi_4O_5I_2$. Reproduced from ref. 142 with permission from Elsevier, copyright 2021. (e) Top-view FESEM of the as-synthesized $Bi_2(CrO_4)_3$ nanoparticles. Reproduced from ref. 144 with permission from Elsevier, copyright 2020. FESEM images of Bi nanostructures synthesized at different temperatures: (f) 50 °C, (g) 70 °C, and (h) 80 °C. Reproduced from ref. 145 with permission from Elsevier, copyright 2012.

However, in chemical reduction methods, many factors including reducing agents, temperature, time, pH, precursor concentration, and surfactants can readily influence nanomaterial size, morphology, and structure, and therefore careful control over these parameters is essential.[143] For instance, Ma *et al.* used NaH_2PO_2 to prepare 1D bismuth nanostructures at low temperature,[145] but they found the dosage of tartaric acid ($H_2C_4H_4O_6$) and reaction temperature significantly affected their morphologies (curled, bundled, and irregular particulate structures were obtained under different conditions, as shown in Fig. 5(f)–(h)).

3.4. Solid phase reaction method

Although hydro/solvothermal methods can precisely control the morphology and size of products, they require substantial water and expensive organic solvents. In contrast, solid-state reactions can overcome these issues through direct mechanical energy absorption during the chemical reaction, also known as mechanochemical synthesis.[131] In solid-state reactions, ground reactant powders undergo solid-state reactions during interparticle contact, eliminating solvent needs and enabling large-scale production.[132] However, direct exposure of nanoparticles to the environment raises safety and environmental concerns with this method.[146] Moreover, uncontrollable preparation conditions lead to relatively broad nanoparticle size distributions.[147] Nevertheless, solid-state reactions have been used for successful synthesis of bismuth-based semiconductors in recent years.[131] For example, Cuéllar *et al.* prepared γ-Bi_2MoO_6 powder from Bi_2O_3 and

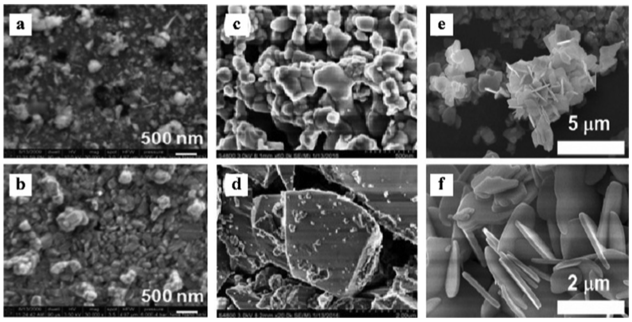

Fig. 6 SEM images of (a) metal films without heat treatment and (b) γ-Bi_2MoO_6 films formed after heat treatment on a glass substrate. Reproduced from ref. 148 with permission from Elsevier, copyright 2011. FESEM images of (c) $Sr_{1-x}Bi_xTi_{1-x}Fe_xO_3$, x = 0.1, (d) x = 0.2. Reproduced from ref. 150 with permission from Elsevier, copyright 2017. (e) and (f) FESEM images of $BiOCl_{1-x}Br_x$ (x = 0.5). Reproduced from ref. 151 with permission from Elsevier, copyright 2023.

MoO_3 at 550 °C, and then fabricated γ-Bi_2MoO_6 films with strong photocatalytic performance *via* thermal decomposition/evaporation.[148] As Fig. 6(a) and (b) show, using this method, heat treatment can promote a densified film and reduced pore size. Additionally, Bijanzad *et al.* used bismuth nitrate and potassium bromide to produce BiOBr nanosheets.[149] With increased preparation time, morphologies transformed from irregular chunks to uniform, thin, and separated nanoplates, which show the ability for photocatalytic rhodamine B and pentachlorophenol degradation.

Beyond basic bismuth compounds, solid-state reactions like grinding or grinding-assisted methods can also prepare heterojunctions and solid solutions to enhance the photoelectric properties of materials.[131] For instance, as Fig. 6(c) and (d) shown, the $SrTiO_3$–$BiFeO_3$ solid solution synthesized by Lu *et al. via* grinding shows high density with 100–1000 nm particle sizes.[150] Compared to $SrTiO_3$, the $SrTiO_3$–$BiFeO_3$ solid solution has a smaller band gap, broader visible light absorption, and stronger photocatalytic hydrogen production. Similarly, $BiOCl_{1-x}Br_x$ nanosheet solid solution synthesized by Thi *et al. via* a simple room temperature water vapor solid-state reaction can significantly improve organic pollutant photocatalytic degradation compared with BiOCl and BiOBr (see Fig. 6(e) and (f)).[151] Additionally, Bi and Bi_2S_3 modified semiconductors usually require two steps including reduction and sulfurization to be prepared, but Bi(Bi_2S_3)/BiOCl heterojunction photocatalyst was successfully synthesized by Shen *et al.* using a one-step room temperature solid-state reaction method and showed high rhodamine B and malachite green degradation efficiency under visible light.[152]

3.5. Sol–gel method

In addition, the sol–gel method is also commonly utilized to synthesize various nanostructures, especially metal oxide nanoparticles. In this approach, metal alkoxide molecular precursors are uniformly mixed in water or alcohol, then hydrolyzed/alcoholized *via* heating and stirring to form a gel. Subsequent steps involve drying and calcining the gel powder to produce nanostructured materials.[153] Compared to other routes, sol–gel offers many advantages like controllable material structures, sizes and surface properties, facile implementation, cost-effectiveness, and high surface areas.[154] In recent years, sol–gel synthesis has been widely applied to bismuth-based compounds. For instance, Sánchez *et al.* used sol–gel methods to prepare BiOCl–TiO_2 composites, where BiOCl micro-flakes were irregularly nested on TiO_2 nanoparticle agglomerates.[155] Moreover, Cui *et al.* recently employed sol–gel spin coating to fabricate sheet-like $Bi_4Ti_3O_{12}$ optoelectronic electrodes, which exhibited high carrier injection efficiency and surface activity after heat treatment.[156] Furthermore, processing sol–gel precursors *via* methods like electrospinning, template deposition, heating, and spin coating can produce nanoparticles with different morphologies such as nanowires, nanotubes, thin films, and spherical nanoparticles.[28] For example, William *et al.* employed sol–gel spin coating to fabricate high-purity $(BiFeO_3)_x$–$(BiCrO_3)_{1-x}$ composite films on glass substrates.[157] Similarly, Xian *et al.* used a polyacrylamide gel approach to synthesize $BiFeO_3$ nanoparticles with varying diameters.[158]

4. Optical and electronic properties and potential applications of bismuth-based materials

4.1. Optoelectronic devices

Bismuth-based semiconductor materials have received significant attention from both academia and industry due to their unique photoelectric properties, which makes them ideal for use in manufacturing optoelectronic devices such as field effect transistors, laser devices, sensors, nanogenerators, and photodetectors.[159] Bi_2S_3, for instance, is widely used in solar cells, optical detection, memristors, and other fields because of its direct band gap, wide visible light range response, and high photoelectric conversion efficiency.[12] As shown in Fig. 7(a)–(c), by using pulsed laser deposition (PLD) technology, Bi_2S_3 quantum dots can be directly deposited on TiO_2 nanorods to prepare quantum dot-sensitized solar cells (QDSSCs), which show strong controllability, high energy conversion efficiency, and excellent stability.[160] In addition to Bi_2S_3, other layered bismuth-based nanomaterials such as Bi_2O_2Se have also been extensively studied in the field of optoelectronics (Fig. 7(d)). Bi_2O_2Se has high air stability, a suitable band gap (~0.8 eV), and high carrier mobility. Photodetectors prepared based on this material show excellent photoelectric characteristics such as a high sensitivity of 65 A W^{-1} at 1200 nm, ultrafast optical response of approximately 1 ps at room temperature, and an inherent bandwidth limit of up to 500 GHz. Researchers also designed a flexible two-dimensional Bi_2O_2Se photodetector array that showed a consistent photoresponse when the substrate bending strain was as high as 1%, confirming that 2D Bi_2O_2Se photodetectors can work on flexible substrates.[161] 2D Bi_2Se_3 flakes, with a narrow band gap of 0.3 eV, have been identified as a promising material for infrared telecommunication photodetectors, as reported by Wang *et al.* Their Bi_2Se_3-based photodetector demonstrates an outstanding on/off

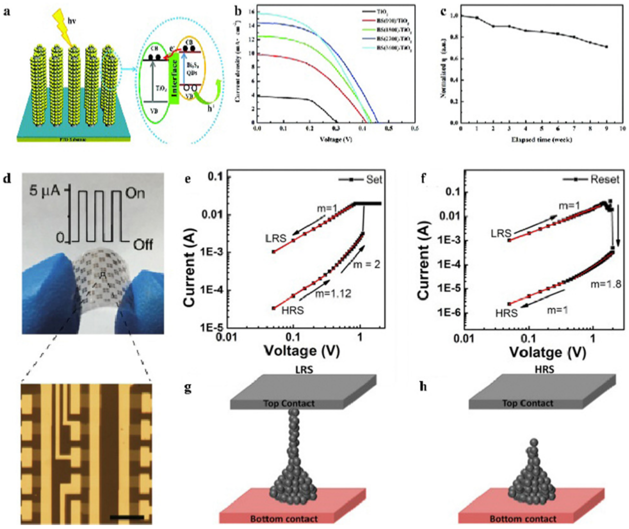

Fig. 7 (a) Illustration of charge separation and transport in the Bi_2S_3-QDSSCs. (b) *J*–*V* characteristics, and (c) time stability of the normalized energy conversion efficiency (η) of QDSSCs assembled with B_2S_3/TiO_2 photoelectrodes. Reproduced from ref. 160 with permission from Royal Society of Chemistry, copyright 2017. (d) Photograph of 2D Bi_2O_2Se photodetector arrays on mica and optical image of 3 × 5 multi-pixel array of 2D Bi_2O_2Se photodetectors. Inset shows photo-response of one typical photodetector when bending the substrate with strain up to 1%. Reproduced from ref. 161 with permission from Springer Nature, copyright 2018. Current–voltage logarithmic plots for (e) set process and (f) reset process; schematic representation of (g) Ag atom mediated conductive filament formation and (h) rupturing of the filament. Reproduced from ref. 164 with permission from Elsevier, copyright 2018.

ratio of 972.5, a high responsivity of 23.8 A W^{-1}, and an impressive external quantum efficiency of 2035%. These remarkable performance metrics suggest that Bi_2Se_3-based photodetectors hold significant potential in communications, military, and remote sensing.[162] Ferroelectric materials such as $BiFeO_3$ with spontaneous polarization characteristics allow for various functions to be realized by adjusting the polarization state of ferroelectric materials through an external electric field. Therefore, resistive switching devices, ferroelectric diodes, and resistive random access memory (RRAM) devices based on ferroelectric materials have been reported.[163] For example, the Ag/$BiFeO_3$/FTO (FTO, fluorine-doped tin oxide) RRAM device with a low-voltage bipolar switch (a maximum on–off ratio of 450) exhibits good reproducibility, robustness, and durability (Fig. 7(e)–(h)),[164] thus resulting in a great potential for storage applications.

4.2. Electrocatalysis

Electrocatalysis is a technology that converts electronic energy into chemical energy by forming chemical bonds.[165] However, the current electrocatalysts predominantly rely on noble metal-based materials like Pt, IrO_2 and RuO, which hinders their widespread application in the field of electrocatalysis.[166] Fortunately, bismuth-based materials show the possibility of being promising alternatives since they are abundant in reserves, easy to synthesize, and exhibit excellent safety and stability, thus providing an opportunity to develop efficient and cost-effective electrocatalysts.[167]

For example, bismuth formate oxide nanowires (BiOCOOH NWS) were synthesized using a simple solvothermal method and reconstituted into ultrathin bismuth nanosheets covered with a thin layer of amorphous oxide (Bi/BiOX NSS) in $KHCO_3$ solution. Compared to rough porous bismuth nanowires (Bi NWs), there are more active sites in the case of Bi/BiOX NSS, leading to stronger CO_2 adsorption and charge transfer ability; thus excellent activity, selectivity, and stability were observed in the electrocatalytic reduction reaction of CO_2 to formate.[168] However, the high energy consumption limits their practicality. To address this issue, as shown in Fig. 8(a)–(c), $Bi_2O_2CO_3$ nanosheets (VO-BOC-NS) with oxygen vacancies reported by Zhang *et al.* exhibited a partial current density of approximately 286 mA cm^{-2} with an operating potential of −0.62 V (*vs.* RHE).[169] More importantly, in a two-electrode electrolyser, only an operating voltage of 2.27 V is required to obtain a current density of 50 mA cm^{-2} and the faradaic efficiency is greater than 90%. This is better than the independent half-reaction and lays the foundation for the practical application of the two-electrode cell in the industry. Similarly, the Bi_1–Co_9–BO_3@450 electrocatalyst was produced by Thomas *et al.* by doping metallic bismuth into cobalt borate, which resulted in the formation of a cooperative catalytic active centre between Bi atoms and Co or B atoms, driving the hydrogen evolution reaction with a current density of 10 mA cm^{-2} and a minimum overpotential of 318 mV (see Fig. 8(d)–(f)).[170] Additionally, it has been reported that $BiFeO_3$ with a twisted perovskite structure exhibits good catalytic performance for the production of NH_3 by nitric acid reduction.[171] The highest faradaic efficiency of this catalyst is 96.85%, and the NH_3 yield is 90.45 mg h^{-1} $mg_{cat}{}^{-1}$. During the nitric acid reduction reaction, crystalline $BiFeO_3$ rapidly transforms into an amorphous phase, which remains stable for a long time in the reaction. In summary, these examples highlight the development of various bismuth-based electrocatalysts and their applications

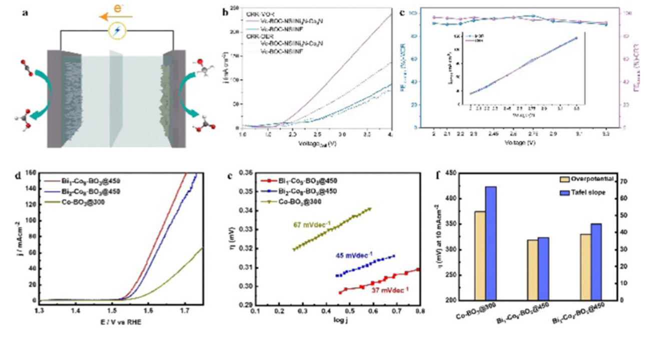

Fig. 8 (a) Schematic diagram of a two-electrode electrolyser. (b) LSV curve. (c) Efficiency of cathode CO_2 reduction reaction (CRR) and anode methanol oxidation reaction (MOR), the inset is the corresponding bias current density. Reproduced from ref. 169 with permission from John Wiley and Sons, copyright 2023. (d) LSV curves of OER over Bi_1–Co_9–BO_3@450, Bi_2–Co_8–BO_3@450, and Co–BO_3@300 (non-doped) catalysts. (e) Their corresponding Tafel slopes. (f) The overpotentials needed for the reaction at 10 mA cm^{-2} *versus* RHE (left) on each catalyst and the corresponding Tafel slopes (right). Reproduced from ref. 170 with permission from John Wiley and Sons, copyright 2023.

for specific reactions, primarily in the context of CO_2 reduction, the hydrogen evolution reaction, and production of NH_3. They also clearly demonstrated the unique properties of bismuth-based electrocatalysts and the importance of designing electrocatalysts with enhanced activity, selectivity, and stability. The established understanding provides a new approach for designing more active and durable electrocatalysts.

4.3. Photocatalysis

As human society continues to develop, non-renewable energy sources such as coal, oil, and natural gas are being rapidly depleted. Environmental pollution and the shortage of renewable energy resources have become two major challenges in the world. To address these issues, the development of clean, renewable energy has become a social priority. Solar energy is one of the most abundant renewable energy sources that can be converted into electronic and chemical energy. Among the various solar energy technologies, photocatalysis, which uses solar energy to drive chemical and energy processes, is a major advancement.[172,173] However, common photocatalytic materials such as TiO_2 with a large band gap and low utilization of visible light limit their application in the field of photocatalysis.[174] Other visible light absorbing photocatalysts also face challenges, with materials like CdS (E_g = ∼2.4 eV) exhibiting rapid radiative recombination of photogenerated electrons and holes and inadequate photo-corrosion resistance.[19] WO_3 (E_g = 2.4–2.8 eV) is constrained by its lower conduction band level, leading to diminished light energy conversion efficiency.[20] Therefore, in recent decades, bismuth-based materials have been explored and have gained popularity in the field of photocatalysis due to their tunable and controllable electronic and optical properties, suitable band edge position, high stability, photo-corrosion resistance, and excellent catalytic performance,[11,17,175] as illustrated in Fig. 9. The recent advancements of bismuth-based photocatalysts are summarized in Table 1 and will be discussed in detail in the following sections. Also, since the compositional space of bismuth-based semiconductors is vast by selecting constituent elements and adjusting element ratio, promising semiconductors with appropriate electronic and optical properties can be explored for specific photocatalytic reactions.

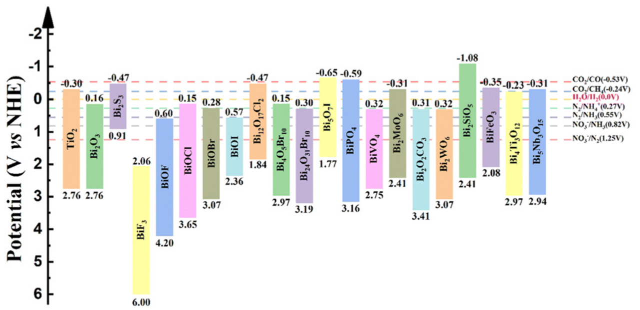

Fig. 9 Band diagram of selected bismuth-based semiconductors and their redox potential of typical reduction reactions. Reproduced from ref. 175 with permission from Royal Society of Chemistry, copyright 2023.

4.3.1. CO_2 reduction. Excessive carbon dioxide emissions and the use of fossil fuels have led to serious environmental problems and energy crises.[11] To eliminate excess CO_2 and reduce the greenhouse effect, the photocatalytic CO_2 reduction technology has emerged,[176] which is a green and efficient way to convert carbon dioxide into renewable hydrocarbon fuels and utilize solar energy to cycle carbon resources.[175] However, low solar energy utilization and catalytic efficiency, as well as low selectivity of CO_2 reduction products, are the main obstacles limiting the development of photocatalytic CO_2 reduction technology.[11,175] To overcome these problems, various bismuth-based photocatalysts have been developed, and significant progress has been made in the field of photocatalytic CO_2 reduction.

Sheng *et al.*[14] prepared a series of bismuth halide perovskite quantum dots $Cs_3Bi_2X_9$ (X = Cl, Br, I) for the photocatalytic reduction of CO_2 to CO at the gas–solid interface. These bismuth-based quantum dot materials have unique structures and excellent optical and electronic properties. Under sunlight irradiation, the CO yield is 134.76 μmol g^{-1}, and the selectivity is as high as 98.7%. Additionally, by controlling the molar ratio of reactants, ultrathin $Bi_4O_5Br_2$ nanosheets ($Bi_4O_5Br_2$-UN) synthesized using the precursor method exhibit as high as 99.5% CO selectivity and 2.3 times higher CO production rate than bulk $Bi_4O_5Br_2$ under UV-visible light irradiation, as shown in Fig. 10(a)–(c).[177] Furthermore, another researcher found that Co-doped $BiVO_4$ can produce about 3 times CH_4 in comparison to undoped $BiVO_4$ because of the new defect levels above the Fermi level.[178] A similar phenomenon was observed by Wang *et al.* in the study of CO_2 reduction over the $BiVO_4/Bi_4Ti_3O_{12}$ heterojunction structure. Because the $BiVO_4/Bi_4Ti_3O_{12}$ heterojunction structure effectively improves the charge separation efficiency and carrier lifetime, a synergistic effect between water oxidation on $Bi_4Ti_3O_{12}$ and CO_2 reduction on $BiVO_4$ is introduced, which can promote the reduction of CO_2 and H_2O to CH_3OH and CO.[179]

4.3.2. Degradation of organic pollutants. The problem of environmental pollution has escalated with the rapid economic growth along with the industrial emissions of various organic pollutants, such as phthalates, polycyclic aromatic hydrocarbons (PAH), phenolic sulfonamides, tetracycline (TC), methylene blue (MB), and rhodamine B, leading to severe consequences for human health and the environment.[180] Photocatalytic technology, recognized as an advanced oxidation process, has emerged as an effective solution for mitigating this issue by harnessing solar energy to decompose and eliminate these harmful pollutants.[181]

Many studies have demonstrated the role of bismuth-based materials in the process of degradation of organic pollutants, especially bismuth oxyhalides. For instance, $Bi_7O_9I_3$ with a unique flaky micro-structure conducts remarkable oxidation capabilities in the degradation of phenol that a 94% removal rate was achieved after just 4 hours of irradiation.[13] Similarly, ultrathin nanosheets of $Bi_4O_5Br_2$ boast a variable energy band structure, which facilitates the generation of oxygen anions and efficient separation of electron–hole pairs. Consequently, these

Table 1 Summary of the photocatalytic activity of bismuth-based semiconductors

Photocatalytic applications	Photocatalyst	Structure or morphology	Photocatalytic performance	Ref.
CO_2 reduction	$Cs_3Bi_2X_9$	Quantum dots	CO yield: 134.76 μmol g^{-1}, CO selectivity: 98.7%	14
	$Bi_4O_5Br_2$	Nanosheets	CO yield: 63.13 μmol g^{-1}, CO selectivity: 99.5%	177
	Co–$BiVO_4$	Co-doped $BiVO_4$	CH_4 production rate: 23.8 μmol g^{-1} h^{-1}	178
	$BiVO_4/Bi_4Ti_3O_{12}$	Heterostructure	CH_3OH and CO production rate: 16.6 and 13.29 μmol g^{-1} h^{-1}	179
Degradation of organic pollutants	$Bi_7O_9I_3$	Hierarchical micro-architecture	Phenol degradation efficiency: 94% after 4 h	13
	$Bi_4O_5Br_2$	Ultrathin nanosheets	CIP degradation efficiency: 75% after 2 h	182
	α/β-Bi_2O_3	Heterostructure	RB 198 and RB 5 degradation efficiency: both 90% after 30 min	184
	Bi_2MoO_6	Nanosheet	CIP and phenol degradation efficiency: 99.4% and 78.6% after 2 h	185
	$BiFeO_3/AgVO_3$	Nanocomposites	RhB degradation efficiency: 70% after 90 min	186
	Bi_3O_4Cl	Ag–Bi_3O_4Cl plasmon	CIP and TBPA degradation efficiency: 93.8% and 94.9% after 2 h	187
Water splitting	$Bi_{24}O_{31}Br_{10}$	Nanoplate	H_2 yield: 133.9 μmol	189
	BP/$BiVO_4$	Heterostructure	H_2 and O_2 production rate: 160 and 102 μmol g^{-1} h^{-1}	190
	Bi_2O_2Se/TiO_2	Heterostructure	H_2 production rate: 1240.7 μmol h^{-1} g^{-1}	191
Artificial nitrogen fixation	Br–BiOCl	Br-doped oxygen vacancy-rich BiOCl micro-sheets	NH_3 production rate: 6.3 μmol h^{-1}	193
	Bi_2MoO_6/BiOBr	Heterostructure	NH_3 yield: 412.18 mol L^{-1}	194
	$(BiO)_2CO_3$	Nanosheets with Au nanoparticles	NH_3 production rate: 38.23 μmol $(cm^{-2}\ h)^{-1}$	195

RB 198 and RB 5: carcinogenic reactive blue 198 and reactive black 5 dyes

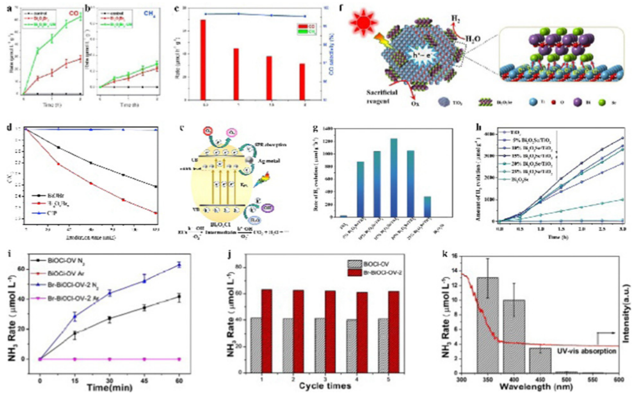

Fig. 10 (a) Rates of CO and CH_4 generation over $Bi_4O_5Br_2$ and $Bi_4O_5Br_2$-UN and (b) under UV-vis light irradiation for 2 h. (c) CO generation and the selectivity over $Bi_4O_5Br_2$-UN under UV-vis light irradiation for 2 h. Reproduced from ref. 177 with permission from Elsevier, copyright 2019. (d) Photocatalytic degradation of CIP in the presence of $Bi_4O_5Br_2$ and BiOBr under visible light irradiation. Reproduced from ref. 182 with permission from Royal Society of Chemistry, copyright 2015. (e) Mechanism of Ag–Bi_3O_4Cl degrading contaminants. Reproduced from ref. 187 with permission from Frontiers, copyright 2023. (f) The scheme of Bi_2O_2Se/TiO_2 for photoreduction of hydrogen evolution. (g) and (h) Rates of H_2 evolution reaction by Bi_2O_2Se, TiO_2 and various Bi_2O_2Se/TiO_2 at room temperature under UV light with 5 vol% of glycerol as a sacrificial reagent. Reproduced from ref. 191 with permission from Elsevier, copyright 2020. (i) NH_3 generation by the as-prepared BiOCl-OV and the Br-BiOCl-OV under Ar and N_2 atmospheres. (j) Cycling stability of BiOCl-OV and Br-BiOCl-OV. (k) N_2 fixation by Br-BiOCl-OV under monochromatic light in compared with its light absorption spectrum. Reproduced from ref. 193 with permission from Elsevier, copyright 2019.

nanosheets demonstrate superior photocatalytic performance compared to BiOBr, particularly in the degradation of the colourless antibiotic ciprofloxacin under visible light as shown in Fig. 10(d).[182] Additionally, various other materials, including Bi_2O_3,[183,184] Bi_2MoO_6,[185] and $BiFeO_3$,[186] have also been investigated for their photocatalytic potential. For instance, Zhang *et al.*[185] prepared small-sized two-dimensional Bi_2MoO_6 nanosheets that exhibited excellent photocatalytic activity, showing a rapid degradation rate for a variety of pollutants under visible light irradiation. Within just 2 hours, impressive degradation rates of 99.4% for ciprofloxacin and 78.6% for phenol were observed with a 20 times higher reaction rate than that of larger bismuth molybdate nanosheets. Moreover, the deposition of metallic silver on the surface of Bi_3O_4Cl (see Fig. 10(e)) significantly enhanced the removal efficiencies of ciprofloxacin and tetrabromobisphenol A (TBPA), reaching 93.8% and 94.9%, respectively. This enhancement can be attributed to the surface plasmon resonance effect of Ag, which inhibits the recombination of electron–hole pairs and simultaneously promotes photocarrier migration and separation to improve both light absorption efficiency and catalytic performance.[187]

4.3.3. Water splitting. Hydrogen (H_2) stands out as a promising secondary energy source due to its numerous advantages, including high energy density, zero carbon emissions, renewability, and the ability to be stored efficiently. Various methods have been investigated to produce H_2, such as steam reforming, coal gasification, and photocatalytic water splitting. Among these, photocatalytic water splitting powered by solar energy is regarded as the greenest and the most efficient technique. Notably, it has the capacity to concurrently generate both H_2 and O_2, underscoring its substantial potential for industrial applications.[188]

The reason of bismuth-based photocatalysts is promising for water splitting lies in their unique electronic properties and band structures. Specifically, the conduction band position of bismuth-based materials, such as $Bi_{24}O_{31}Br_{10}$, has been found to meet the potential requirements for decomposing water into H_2 through first-principles calculations by Shang *et al.*,[189] which agrees well with experimental observations that $Bi_{24}O_{31}Br_{10}$ has a certain photocatalytic water splitting ability, with 133.9 μmol of H_2 precipitated from $Bi_{24}O_{31}Br_{10}$ after 40 hours of visible light irradiation. In addition, Zhu *et al.*[190] reported a new BP/$BiVO_4$ two-dimensional heterostructure photocatalyst, which has a staggered band structure facilitating charge separation allowing water to be reduced and oxidized on BP and $BiVO_4$, respectively. The optimal H_2 and O_2 yields over the BP/$BiVO_4$ catalyst are approximately 160 and 102 μmol g^{-1} h^{-1}, respectively, without using any sacrificial agent or external bias. To further improve the photocatalytic activity, researchers deposited bismuth selenide oxide (Bi_2O_2Se) on TiO_2 nanoparticles, which significantly suppressed the recombination of photogenerated electrons and holes in Bi_2O_2Se/TiO_2 compared to pure TiO_2. The hydrogen production rate of Bi_2O_2Se/TiO_2 is 1240.7 μmol h^{-1} g^{-1}, which is about 50 times higher than that of pure TiO_2 (see Fig. 10(f)–(h)).[191]

4.3.4. Artificial nitrogen fixation. Ammonia is a crucial raw material in the production of fertilizers, chemicals, and energy. However, the traditional ammonia synthesis process has many drawbacks, such as high temperature, high pressure, and a large amount of CO_2 emissions. As a result, researchers have to explore new sustainable alternatives and find photocatalytic nitrogen fixation for ammonia synthesis can be a candidate.[192]

To address the commonly encountered problems of slow carrier transmission and low surface reaction efficiency in the photocatalytic synthesis of ammonia, Wu *et al.* reported that Br-doped oxygen vacancy-rich BiOCl micro-sheets (Br-BiOCl-OV) were synthesized using a solvothermal method and ion exchange treatment, which exhibits a high charge separation efficiency and ammonia generation rate (6.3 μmol h^{-1}) under visible light irradiation, indicating a stable N_2 fixation ability, as illustrated in Fig. 10(i)–(k).[193] Moreover, Zhang *et al.*[194] introduced bismuth vacancies into the surface of BiOBr nanospheres with oxygen vacancies and constructed a Bi_2MoO_6/BiOBr composite structure. The synergistic effect of bismuth vacancies and oxygen vacancies significantly improves the efficiency of photogenerated electron–hole pairs and the light absorption capability of the composite material. The hierarchical Bi_2MoO_6/BiOBr nanosheet assembly structure is beneficial to the surface adsorption and activation of N_2 on the catalyst leading to a four times higher yield of NH_3 under visible light irradiation than BiOBr with oxygen vacancies. On the other hand, Xiao *et al.*[195] found that gold nanoparticles and $(BiO)_2CO_3$ nanosheets also have a strong synergistic effect that can break the strong triple bond of nitrogen to form ammonia. Because modification of $(BiO)_2CO_3$ nanosheets with gold nanoparticles not only generates hot electrons but also significantly enhances light capture and charge separation efficiency, thereby improving the conversion efficiency of photocatalytic nitrogen oxidation.

4.4. Cancer treatment and diagnostic imaging

In recent years, there has been a surge of interest in the use of bismuth-based nanomaterials due to their promising applications and potential for clinical use, such as combined tumour therapy, multi-modal imaging, antibacterial activities, and biosensing.[196] For example, Li *et al.*[197] investigated the use of bismuth sulfide nanorods (Bi_2S_3 NRs) as contrast agents (CAs) for dual-energy computed tomography (DECT) (see Fig. 11(a)). The results showed that the X-ray attenuation characteristics of Bi_2S_3 NRs in dual-energy imaging were superior to those of clinically commonly used iohexanol, particularly at higher energies. Additionally, Bi_2S_3 NRs exhibited a high photothermal conversion rate and could be utilized for photothermal therapy (PTT) under the guidance of DECT imaging to destroy osteosarcoma cells and inhibit tumour growth. Overall, the combination of DECT imaging and photothermal therapy strategies using Bi_2S_3 NRs as contrast agents holds great potential for the treatment of bone diseases. Bi_2Se_3 also exhibits significant promise in cancer treatment, demonstrated by the successful development of an efficient colorimetric biosensor utilizing highly catalytic active Bi_2Se_3 nanosheets decorated with Au nanoparticles (Au/Bi_2Se_3), as shown in Fig. 11(b). This innovative approach serves as an alternative method for cancer diagnosis. The intrinsic low redox potential and distinctive topological insulating properties of Bi_2Se_3 nanosheets enable the provision and accumulation of electrons on their surface,

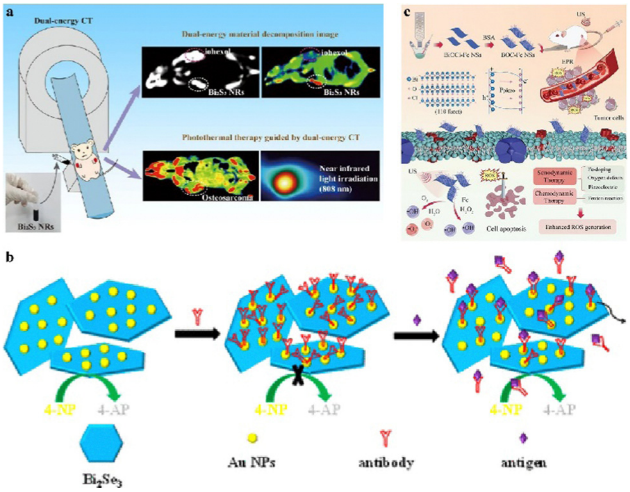

Fig. 11 (a) Schematic diagram of Bi_2S_3 nanorods for DECT-guided photothermal treatment of osteosarcoma. Reproduced from ref. 197 with permission from Springer Nature, copyright 2023. (b) Schematic illustration of a versatile and colorimetric biosensor based on the tunable smart interface of catalytic Au/Bi_2Se_3 nanosheets. Reprinted with permission from ref. 198. Copyright 2017 American Chemical Society. (c) Schematic diagram of iron-doped bismuth chloride nanosheets for enhanced tumour sonodynamic therapy (SDT). Reproduced from ref. 199 with permission from John Wiley and Sons, copyright 2023.

which fosters robust synergistic catalytic effects in conjunction with Au nanoparticles. The resulting sensor exhibits exceptional sensitivity and selectivity for cancer biomarkers.[198] In addition, a novel type of ultrathin iron-doped bismuth chloride nanosheets (BOC-Fe NSs) was demonstrated to be a highly efficient sonosensitizer for tumour treatment through sonodynamic therapy, as shown in Fig. 11(c).[199] The iron-doped bismuth chloride nanosheets with specific oxygen vacancies can act as electron capture sites to promote the generation of reactive oxygen species (ROS) under the influence of ultrasonic waves. The toxic ROS produced can effectively kill cancer cells. Both *vitro* and *vivo* experimental studies indicate that the prepared BOC-Fe NSs can effectively inhibit the growth of breast cancer cells. The successful development of BOC-Fe NSs provides a new nano-sonosensitizer option for SDT treatment of cancer.

5. Concluding remarks and outlook

Bismuth-based semiconductor materials have attracted significant attention from both academia and industry due to their unique electronic and optical properties. The studies on these materials are not only the cutting edge of scientific research but also the hotspot for industrial applications owing to their cost-effectiveness, environmental friendliness, and sustainability. To provide an understanding of how to modify and efficiently utilize these unique bismuth-based materials so that they can be applied to more fields, a comprehensive introduction to their crystal structures, electronic structures, photoelectric characteristics, modification techniques, and commonly employed synthesis methods as well as potential applications in electrocatalysis, photocatalysis, and medical fields is given.

Firstly, since bismuth-based semiconductor materials commonly encounter several challenges that impact their performance (such as high rates of photogenerated electron–hole recombination, limited capacity to absorb visible light, and susceptibility to chemical instability), low photoelectric conversion efficiency quite restricts their practical applications. Therefore, various modification techniques (including metal ion doping, morphology regulation, and the construction of heterostructures) are introduced to overcome these problems. Through these approaches, it becomes possible to optimize the band structure, enhance light absorption capabilities, and improve carrier separation efficiency. Specifically, with regard to certain bismuth-based semiconductors with layered structures, it is needful to explore the hierarchical porous structure concept because this kind of innovative morphology can increase the diffusion of reactants and provide additional reaction sites, leading to enhanced absorption of incident light. Ultimately, these enhancements significantly contribute to improved photoelectric performance and increased photoelectric conversion efficiency. These refined methodologies offer valuable guidance and direction for the continued development and practical utilization of bismuth-based semiconductors.

Secondly, although various synthesis methods have been developed for bismuth-based semiconductors, these approaches still show inherent shortcomings and require further refinement. For instance, the solid-state reaction method faces challenges in adjusting the microstructure and morphology of bismuth-based materials, while the hydrothermal/solvothermal method suffers from limitations in production efficiency and the inability to facilitate large-scale manufacturing. Additionally, during the design and synthesis of bismuth-based semiconductors, it is also imperative to consider factors such as safety, environmental sustainability, and economic viability. Particularly in the industry, the demand to synthesize bismuth-based semiconductors with outstanding photoelectric properties using a straightforward, large-scale, and high-yield approach is still a substantial challenge.

Moreover, in recent years, remarkable advancements in bismuth-based semiconductors have been witnessed, particularly in the realm of photocatalysis. However, it is important to note that despite these achievements, many photocatalytic technologies are stuck in the experimental investigation section and fall short of meeting the demands of practical production applications. In addition, the complicated photocatalytic reaction mechanism still needs further deep investigation for optimization of photocatalysts to achieve excellent performance. Therefore, building an understanding of the effect of electronic structure or bulk composition of materials on their photocatalytic performance, and unraveling the kinetics of electron transfer and surface chemistry in photocatalytic reactions, are the critical questions asked in the community. Based on these studies, expanding beyond photocatalysis, bismuth-based semiconductors will hold more potential for diverse applications in biological, medical, and other domains. For example, since bismuth possesses exceptional antibacterial properties, bismuth-based compounds will present more chances in the field of photocatalytic bacterial inactivation (such as treating ulcers and bacterial infections) compared with other photocatalysts. They can also be integrated with electrochemical technology to foster the development of novel biosensors and detection devices, capable of identifying cells, organic molecules. Additionally, their utility can also be extended to the field of thin-film technology for high-efficiency photoelectric conversion and storage devices or in the field of biotechnology as promising candidates with a high photothermal conversion rate for the applications of photodynamic therapy and photothermal therapy.

Author contributions

Conceptualization, T. Z.; writing – original draft preparation, P. X., and Y. S.; writing – review & editing, Y. L., M. L., C. Y. and X. Z.; supervision, T. Z.; project administration, T. Z.

Conflicts of interest

The authors declare no conflict of interest.

Acknowledgements

Funding: This research was funded by NSFC (grant no. 22102023 and 62275047), the National Key R&D Program of China (grant no. 2021YFB2800700), the Natural Science Foundation of Jiangsu Province (grant BK20220816) and the fellowship of China Postdoctoral Science Foundation (grant no. 2021M700768 and 2022M710672).

Notes and references

1 B. Biswas and B. Saha, *Phys. Rev. Mater.*, 2019, **3**, 25.
2 B. Du, J. L. Hudgins, E. Santi, A. T. Bryant, P. R. Palmer and H. A. Mantooth, *IEEE Trans. Power Electron.*, 2010, **25**, 237–248.
3 A. Zakutayev, *J. Mater. Chem. A*, 2016, **4**, 6742–6754.
4 Z. N. Guo, R. Cao, H. D. Wang, X. Zhang, F. X. Meng, X. Chen, S. Y. Gao, D. K. Sang, T. H. Nguyen, A. T. Duong, J. L. Zhao, Y. J. Zeng, S. Cho, B. Zhao, P. H. Tan, H. Zhang and D. Y. Fan, *Natl. Sci. Rev.*, 2022, **9**, nwab098.
5 J. R. Chen, F. X. Qiu, W. Z. Xu, S. S. Cao and H. J. Zhu, *Appl. Catal., A*, 2015, **495**, 131–140.
6 X. Q. Ji, C. Lu, Z. Y. Yan, L. Shan, X. Yan, J. J. Wang, J. Y. Yue, X. H. Qi, Z. Liu, W. H. Tang and P. G. Li, *J. Phys. D: Appl. Phys.*, 2022, **55**, 443002.
7 D. Wang, X. B. Li and H. B. Sun, *Nano Lett.*, 2021, **21**, 6298–6303.
8 W. H. Lee and Y. D. Park, *Polymers*, 2014, **6**, 1057–1073.
9 P. Chen, W. J. Ong, Z. Shi, X. Zhao and N. Li, *Adv. Funct. Mater.*, 2020, **30**, 1909667.
10 S. Y. Yu, L. Zhang, L. B. Zhu, Y. Gao, G. C. Fan, D. M. Han, G. Chen and W. W. Zhao, *Coord. Chem. Rev.*, 2019, **393**, 9–20.
11 X. Liu, J. Xiao, S. Ma, C. Shi, L. Pan and J. J. Zou, *ChemNanoMat*, 2021, **7**, 684–698.
12 Y. L. Zhou, H. S. Yin and S. Y. Ai, *TrAC, Trends Anal. Chem.*, 2023, **158**, 116876.
13 X. Xiao and W. D. Zhang, *RSC Adv.*, 2011, **1**, 1099–1105.
14 J. Sheng, Y. He, J. Li, C. Yuan, H. Huang, S. Wang, Y. Sun, Z. Wang and F. Dong, *ACS Nano*, 2020, **14**, 13103–13114.
15 X. Xiao and W. Zhang, *RSC Adv.*, 2011, **1**, 1099–1105.
16 X. Liu, J. Xiao, S. Ma, C. Shi, L. Pan and J. Zou, *ChemNanoMat*, 2021, **7**, 684–698.
17 X. Meng and Z. Zhang, *J. Mol. Catal. A: Chem.*, 2016, **423**, 533–549.
18 S. Sun and W. Wang, *RSC Adv.*, 2014, **4**, 47136–47152.
19 F. Ma, Y. Wu, Y. Shao, Y. Zhong, J. Lv and X. Hao, *Nano Energy*, 2016, **27**, 466–474.
20 Z. Zhao and M. Miyauchi, *Angew. Chem., Int. Ed.*, 2008, **47**, 7051–7055.
21 G. Dai, J. Yu and G. Liu, *J. Phys. Chem. C*, 2012, **116**, 15519–15524.
22 L. Chen, J. He, Y. Liu, P. Chen, C. Au and S. Yin, *Chin. J. Catal.*, 2016, **37**, 780–791.
23 S. C. Wang, L. Z. Wang and W. Huang, *J. Mater. Chem. A*, 2020, **8**, 24307–24352.
24 K. Qin, Q. Zhao, H. Yu, X. Xia, J. Li, S. He, L. Wei and T. An, *Environ. Res.*, 2021, **199**, 111360.
25 L. Zhang, Y. Li, Q. Li, J. Fan, S. A. C. Carabineiro and K. Lv, *Chem. Eng. J.*, 2021, **419**, 129484.
26 R. Kumar, P. Raizada, N. Verma, A. Hosseini Bandegharaei, V. K. Thakur, Q. V. Le, V. H. Nguyen, R. Selvasembian and P. Singh, *J. Cleaner Prod.*, 2021, **297**, 126617.
27 S. Song, Z. Xing, H. Zhao, Z. Li and Z. Wei, *Green Energy Environ.*, 2023, **8**, 1232–1264.
28 P. Sivasubramanian, J. H. Chang, S. Nagendran, C. D. Dong, M. Shkir and M. Kumar, *Chemosphere*, 2022, **307**, 135652.
29 R. a He, S. Cao, P. Zhou and J. Yu, *Chin. J. Catal.*, 2014, **35**, 989–1007.
30 R. He, D. Xu, B. Cheng, J. Yu and W. Ho, *Nanoscale Horiz.*, 2018, **3**, 464–504.
31 R. A. He, S. W. Cao and J. G. Yu, *Acta Phys.-Chim. Sin.*, 2016, **32**, 2841–2870.
32 R. Kumar, P. Raizada, N. Verma, A. Hosseini-Bandegharaei, V. K. Thakur, L. Quyet Van, N. Van-Huy, R. Selvasembian and P. Singh, *J. Cleaner Prod.*, 2021, **297**, 126617.
33 J. Xiong, P. Song, J. Di, H. Li and Z. Liu, *J. Mater. Chem. A*, 2019, **7**, 25203–25226.
34 M. Li, H. Huang, S. Yu, N. Tian and Y. Zhang, *ChemCatChem*, 2018, **10**, 4477–4496.
35 K. Xu, L. Wang, X. Xu, S. X. Dou, W. Hao and Y. Du, *Energy Storage Mater.*, 2019, **19**, 446–463.
36 L. Sun, M. Hu, M. Liang, Y. Wu and L. Liu, *Chem. Ind. Eng. Prog.*, 2022, **41**, 4813–4830.
37 R. Sharma, M. Khanuja, S. N. Sharma and O. P. Sinha, *Int. J. Hydrogen Energy*, 2017, **42**, 20638–20648.
38 A. H. Zahid and Q. Han, *Nanoscale*, 2021, **13**, 17687–17724.
39 L. S. Zhang, W. Z. Wang, J. O. Yang, Z. G. Chen, W. Q. Zhang, L. Zhou and S. W. Liu, *Appl. Catal., A*, 2006, **308**, 105–110.
40 B. Yu, *Chem. Eng. J.*, 2018, **32**, 57–61.
41 W. Zou, W. C. Hao, X. Xin and T. M. Wang, *Chin. J. Inorg. Chem.*, 2009, **25**, 1971–1976.
42 T. Karnan and S. Samuel, *Ceram. Int.*, 2016, **42**, 4779–4787.
43 S. D. Khairnar and V. S. Shrivastava, *SN Appl. Sci.*, 2019, **1**, 762.
44 Q. Hao, R. T. Wang, H. J. Lu, C. A. Xie, W. H. Ao, D. M. Chen, C. Ma, W. Q. Yao and Y. F. Zhu, *Appl. Catal., B*, 2017, **219**, 63–72.
45 T. P. Xie, J. Yang, Y. Penga, J. K. Wang, S. L. Liu, L. J. Xu and C. L. Liu, *Mater. Technol.*, 2019, **34**, 843–850.
46 M. Chen, J. T. Bi, X. Huang, T. Wang, Z. Wang and H. X. Hao, *Chemosphere*, 2021, **278**, 130386.
47 S. M. Wang, Y. Guan, R. H. Zeng, Z. J. Zhang, L. Liu, Z. Y. Li, W. An and Y. Fu, *ChemSusChem*, 2019, **12**, 4874–4881.
48 Q. Yang, J. B. Zhong, J. Z. Li, J. F. Chen, Z. Xiang, T. Wang and M. J. Li, *Curr. Appl. Phys.*, 2017, **17**, 484–487.
49 K. S. Al-Namshah and R. M. Mohamed, *Appl. Nanosci.*, 2018, **8**, 1233–1239.
50 J. A. Zhu, S. H. Wang, J. U. Wang, D. Q. Zhang and H. X. Li, *Appl. Catal., B*, 2011, **102**, 120–125.

51 D. Kim and D. Jung, *Chem. Phys. Lett.*, 2017, **674**, 130–135.

52 H. Lu, Q. Hao, T. Chen, L. Zhang, D. Chen, C. Ma, W. Yao and Y. Zhu, *Appl. Catal., B*, 2018, **237**, 59–67.

53 S. Majumder, N. D. Quang, T. T. Hien, N. D. Chinh, H. Yang, C. Kim and D. Kim, *J. Alloys Compd.*, 2021, **870**, 159545.

54 G. S. Jiang, X. D. Zhang, C. Liu, H. Ma, H. Yu and F. Wang, *Vacuum*, 2020, **181**, 109759.

55 Y. N. Bai, T. Y. Ouyang, X. R. Li, Y. W. Yan, Z. S. Kong, X. L. Ma, Z. Li, Z. D. Li, X. M. Cai, J. M. Cai and H. L. Tan, *J. Alloys Compd.*, 2023, **933**, 167814.

56 H. F. Bao, X. Q. Cui, C. M. Li, Y. Gan, J. Zhang and J. Guo, *J. Phys. Chem. C*, 2007, **111**, 12279–12283.

57 P. Hu, Y. Cao and B. Lu, *Mater. Lett.*, 2013, **106**, 297–300.

58 Y. Zhou, M. Wang, Z. Yang, H. Yin and S. Ai, *Sens. Actuators, B*, 2015, **206**, 728–734.

59 Z. M. Li and Y. Tian, *Photonics*, 2022, **9**, 790.

60 J. Gao, Y. Ding, K. Yan and J. Zhang, *J. Mater. Chem. B*, 2022, **10**, 3524–3530.

61 M. Wang, Y. Xue, J. H. Zhu, A. J. Wang, L. P. Mei and P. Song, *New J. Chem.*, 2021, **45**, 22833–22838.

62 M. Ganapathy, Y. Hsu, J. Thomas, L. Y. Chen, C. T. Chang and V. Alagan, *Energy Fuels*, 2021, **35**, 14995–15004.

63 Y. Bessekhouad, D. Robert and J. V. Weber, *J. Photochem. Photobiol., A*, 2004, **163**, 569–580.

64 X. Li, R. Huang, Y. Hu, Y. Chen, W. Liu, R. Yuan and Z. Li, *Inorg. Chem.*, 2012, **51**, 6245–6250.

65 I. M. Kobasa and G. P. Tarasenko, *Theor. Exp. Chem.*, 2002, **38**, 255–258.

66 S. Zheng, Z. Li, T. Lu, J. Wang, Y. Wang, Y. Cui, Z. Zhang, M. He and B. Song, *Comput. Theor. Chem.*, 2023, **1225**, 114170.

67 H. Steinberg, D. R. Gardner, Y. S. Lee and P. Jarillo-Herrero, *Nano Lett.*, 2010, **10**, 5032–5036.

68 R. He, S. Ou, Y. Liu, Y. Liu and D. Xu, *Chin. J. Catal.*, 2022, **43**, 370–378.

69 J. Lei, N. Qie, J. Zhou, Y. Hua and T. Ji, *Mater. Lett.*, 2012, **83**, 108–111.

70 Y. H. Chuai, Y. F. Wang and Y. Bai, *Opt. Mater.*, 2023, **140**, 113804.

71 D. Li, J. Lao, C. Jiang, C. Luo, R. Qi, H. Lin, R. Huang, G. I. N. Waterhouse and H. Peng, *Int. J. Hydrogen Energy*, 2019, **44**, 30876–30884.

72 Z. M. Yuan and Z. Y. Jiang, *Molecules*, 2023, **28**, 4400.

73 Z. Zhao and W. Dai, *Inorg. Chem.*, 2014, **53**, 13001–13011.

74 Z. Wang, Z. Chu, C. Dong, Z. Wang, S. Yao, H. Gao, Z. Liu, Y. Liu, B. Yang and H. Zhang, *ACS Appl. Nano Mater.*, 2020, **3**, 1981–1991.

75 H. An, Y. Du, T. Wang, C. Wang, W. Hao and J. Zhang, *Rare Met.*, 2008, **27**, 243–250.

76 X. M. Chen, P. Y. Chen, S. M. Yang and H. W. Gao, *Nanotechnology*, 2023, **34**, 052001.

77 W. L. Huang and Q. Zhu, *Comput. Mater. Sci.*, 2008, **43**, 1101–1108.

78 L. Zhao, X. Zhang, C. Fan, Z. Liang and P. Han, *Phys. B*, 2012, **407**, 3364–3370.

79 Y. Liu, B. Yang, H. He, S. Yang, X. Duan and S. Wang, *Sci. Total Environ.*, 2022, **804**, 150215.

80 K. L. Zhang, C. M. Liu, F. Q. Huang, C. Zheng and W. D. Wang, *Appl. Catal., B*, 2006, **68**, 125–129.

81 X. Zhang, R. Li, M. Jia, S. Wang, Y. Huang and C. Chen, *Chem. Eng. J.*, 2015, **274**, 290–297.

82 X. Xiao, J. Jiang and L. Zhang, *Appl. Catal., B*, 2013, **142–143**, 487–493.

83 J. Zhang, J. Wu, P. Lu, Q. Liu, T. Huang, H. Tian, R. Zhou, J. Ren, B. Yuan, X. Sun and W. Zhang, *Mater. Lett.*, 2017, **186**, 353–356.

84 M. Zhao, C. Q. Fu, K. J. Wang, Y. Zhang, Y. M. Xia, Q. Zhang, C. D. Li, M. C. Liu, Z. H. Zhang and W. J. Wang, *J. Alloys Compd.*, 2021, **852**, 156698.

85 X. Su and D. Wu, *Mater. Sci. Semicond. Process.*, 2018, **80**, 123–130.

86 M. T. Le, J. Van Craenenbroeck, I. Van Driessche and S. Hoste, *Appl. Catal., A*, 2003, **249**, 355–364.

87 D. H. He, W. Ueda and Y. Moro-Oka, *Catal. Lett.*, 1992, **12**, 35–44.

88 A. Bhakoo, G. C. Bond, R. D. Rees, B. Sauerhammer, A. O. Taylor and I. York, *Catal. Lett.*, 1999, **57**, 55–60.

89 C. Q. Zhang, Q. Zhou, C. Xu, X. Liu, Y. Tan and W. Y. Huang, *Nonferrous Met. Mater. Eng.*, 2021, **12**, 56–65.

90 Y. F. Zhao, Q. Y. Mao, X. Y. Zhai and G. Y. Zhang, *Prog. Chem.*, 2021, **33**, 1331–1343.

91 Y. Jia, Y. Lin, Y. Ma and W. Shi, *Mater. Lett.*, 2019, **234**, 83–86.

92 D. D. Wang, Z. X. Lin, H. J. Gu and H. Y. Li, *Prog. Chem.*, 2023, **35**, 606–619.

93 B. Senthilkumar, R. K. Selvan, L. Vasylechko and M. Minakshi, *Solid State Sci.*, 2014, **35**, 18–27.

94 K. Lai, W. Wei, Y. Zhu, M. Guo, Y. Dai and B. Huang, *J. Solid State Chem.*, 2012, **187**, 103–108.

95 Y. X. Qin, S. C. Liu, X. Shen, H. Y. Gui and Y. N. Bai, *J. Alloys Compd.*, 2022, **894**, 162534.

96 M. Z. Sun, P. Y. Guo, M. Wang and F. Y. Ren, *Optik*, 2019, **199**, 163319.

97 S. N. Lou, J. Scott, A. Iwase, R. Amal and Y. H. Ng, *J. Mater. Chem. A*, 2016, **4**, 6964–6971.

98 Y. P. Zhou, W. Y. Jiao, Y. Xie, F. He, Y. Ling, Q. Yang, J. S. Zhao, H. Ye and Y. Hou, *J. Colloid Interface Sci.*, 2022, **608**, 2213–2223.

99 J. L. Li, X. J. Liu, Z. Sun and L. K. Pan, *Ceram. Int.*, 2015, **41**, 8592–8598.

100 A. Phuruangrat, S. Buapoon, T. Bunluesak, P. Suebsom, S. Thongtem and T. Thongtem, *J. Aust. Ceram. Soc.*, 2022, **58**, 71–82.

101 A. Phuruangrat, P. Dumrongrojthanath, S. Thongtem and T. Thongtem, *Mater. Lett.*, 2017, **194**, 114–117.

102 Z. Dai, F. Qin, H. P. Zhao, F. Tian, Y. L. Liu and R. Chen, *Nanoscale*, 2015, **7**, 11991–11999.

103 L. N. Wang, X. Q. Shi, Y. F. Jia, H. F. Cheng, L. Wang and Q. Z. Wang, *Chin. Chem. Lett.*, 2021, **32**, 1869–1878.

104 S. Gofurov, N. Uezono, L. G. Oktariza, J. Q. Liu, S. Pawar, M. M. Islam and T. Sakurai, *Jpn. J. Appl. Phys.*, 2023, **62**, SK1051.

105 T. D. Nguyen, V. H. Nguyen, S. Nanda, D. V. N. Vo, V. H. Nguyen, T. V. Tran, L. X. Nong, T. T. Nguyen, L. G. Bach, B. Abdullah, S. S. Hong and T. V. Nguyen, *Environ. Chem. Lett.*, 2020, **18**, 1779–1801.

106 A. Ul Islam, M. N. H. Liton, H. M. T. Islam, M. Al Helal and M. Kamruzzaman, *Chin. Phys. B*, 2017, **26**, 036301.

107 Z. Zhao, Z. Li and Z. Zou, *Phys. Chem. Chem. Phys.*, 2011, **13**, 4746–4753.

108 A. Kudo, K. Omori and H. Kato, *J. Am. Chem. Soc.*, 1999, **121**, 11459–11467.

109 G. S. Kamble, T. S. Natarajan, S. S. Patil, M. Thomas, R. K. Chougale, P. D. Sanadi, U. S. Siddharth and Y. C. Ling, *Nanomaterials*, 2023, **13**, 1528.

110 J. Su, L. Guo, N. Bao and C. A. Grimes, *Nano Lett.*, 2011, **11**, 1928–1933.

111 Y. Liu, B. Huang, Y. Dai, X. Zhang, X. Qin, M. Jiang and M. H. Whangbo, *Catal. Commun.*, 2009, **11**, 210–213.

112 S. Okunaka, H. Kameshige, S. Oozu, K. Sayama and H. Tokudome, *Jpn. J. Appl. Phys.*, 2023, **62**, SK1030.

113 K. Ding, B. Chen, Z. Fang, Y. Zhang and Z. Chen, *Phys. Chem. Chem. Phys.*, 2014, **16**, 13465–13476.

114 X. Zhang, Y. Huang, F. Ma, Z. Zhang and X. Wei, *J. Phys. Chem. Solids*, 2018, **121**, 85–92.

115 Y. Hu, D. Li, Y. Zheng, W. Chen, Y. He, Y. Shao, X. Fu and G. Xiao, *Appl. Catal., B*, 2011, **104**, 30–36.

116 H. Y. Jiang, J. H. He, C. Y. Deng, X. D. Hong and B. Liang, *Molecules*, 2022, **27**, 8698.

117 J. Ning, J. Zhang, R. Dai, Q. Wu, L. Zhang, W. B. Zhang, J. F. Yan and F. C. Zhang, *Appl. Surf. Sci.*, 2022, **579**, 152219.

118 A. Elaouni, M. El Ouardi, A. BaQais, M. Arab, M. Saadi and H. Ait Ahsaine, *RSC Adv.*, 2023, **13**, 17476–17494.

119 Y. Liang and J. W. Shi, *J. Inorg. Organomet. Polym. Mater.*, 2020, **30**, 2872–2880.

120 T. Chen, L. Liu, C. Hu and H. Huang, *Chin. J. Catal.*, 2021, **42**, 1413–1438.

121 K. Lai, W. Wei, Y. Dai, Z. Ruiqin and B. Huang, *Rare Met.*, 2011, **30**, 166–172.

122 K. Akihiko and H. Satoshi, *Chem. Lett.*, 1999, 1103–1104.

123 L. Zhang and Y. Zhu, *Catal. Sci. Technol.*, 2012, **2**, 694–706.

124 S. Murcia-López, M. C. Hidalgo and J. A. Navío, *Photochem. Photobiol.*, 2013, **89**, 832–840.

125 Y. H. Zhang and Y. J. Xu, *RSC Adv.*, 2014, **4**, 2904–2910.

126 J. Ren, W. Wang, L. Zhang, J. Chang and S. Hu, *Catal. Commun.*, 2009, **10**, 1940–1943.

127 X. Guo, D. Wu, X. Long, Z. Zhang, F. Wang, G. Ai and X. Liu, *Mater. Charact.*, 2020, **163**, 110297.

128 S. Bera, S. Samajdar, S. Pal, P. S. Das, L. A. H. Jones, H. Finch, V. R. Dhanak and S. Ghosh, *Ceram. Int.*, 2022, **48**, 35814–35824.

129 M. Shang, W. Wang, L. Zhang, S. Sun, L. Wang and L. Zhou, *J. Phys. Chem. C*, 2009, **113**, 14727–14731.

130 Y. Yang, R. Z. Ouyang, L. N. Xu, N. Guo, W. W. Li, K. Feng, L. Ouyang, Z. Y. Yang, S. Zhou and Y. Q. Miao, *J. Coord. Chem.*, 2015, **68**, 379–397.

131 Q. F. Han, *Chem. Eng. J.*, 2021, **414**, 127877.

132 M. Xu, J. Yang, C. Sun, L. Liu, Y. Cui and B. Liang, *Chem. Eng. J.*, 2020, **389**, 124402.

133 S. Su, Q. Han, X. Wang and J. Zhu, *Appl. Surf. Sci.*, 2018, **455**, 616–621.

134 J. Jiang, K. Zhao, X. Xiao and L. Zhang, *J. Am. Chem. Soc.*, 2012, **134**, 4473–4476.

135 Y. Lin, C. Lu and C. Wei, *J. Alloys Compd.*, 2019, **781**, 56–63.

136 C. B. Zhang, X. P. Tao, W. C. Jiang, J. X. Guo, P. F. Zhang, C. Li and R. G. Li, *Acta Phys.-Chim. Sin.*, 2024, **40**, 2303034.

137 B. Wang, L. Guo and T. He, *RSC Adv.*, 2016, **6**, 30115–30124.

138 W. Shi, M. Li, X. Huang, H. Ren, F. Guo, Y. Tang and C. Lu, *Chem. Eng. J.*, 2020, **394**, 125009.

139 Y. Huo, J. Zhang, M. Miao and Y. Jin, *Appl. Catal., B*, 2012, **111–112**, 334–341.

140 J. Di, J. Xia, H. Li, S. Guo and S. Dai, *Nano Energy*, 2017, **41**, 172–192.

141 Y. Huang, Y. Zhu, S. Chen, X. Xie, Z. Wu and N. Zhang, *Adv. Sci.*, 2021, **8**, 2003626.

142 L. P. Chen, C. E. Li, Y. F. Zhao, J. Wu, X. K. Li, Z. W. Qiao, P. He, X. M. Qi, Z. H. Liu and G. Q. Wei, *Chem. Eng. J.*, 2021, **425**, 131599.

143 S. S. Wu, Z. F. Xu, J. L. Zhang and M. S. Zhu, *Sol. RRL*, 2021, **5**, 2100668.

144 M. A. Hamza, A. N. El-Shazly, S. A. Tolba and N. K. Allam, *Chem. Eng. J.*, 2020, **384**, 123351.

145 D. Ma, J. Zhao, Y. Zhao, X. Hao and Y. Lu, *Chem. Eng. J.*, 2012, **209**, 273–279.

146 F. Gottschalk and B. Nowack, *J. Environ. Monit.*, 2011, **13**, 1145–1155.

147 B. Stieberova, M. Zilka, M. Ticha, F. Freiberg, P. Caramazana-González, J. McKechnie and E. Lester, *J. Cleaner Prod.*, 2019, **241**, 118325.

148 E. L. Cuéllar, A. Martínez-de la Cruz, K. H. L. Rodríguez and U. O. Méndez, *Catal. Today*, 2011, **166**, 140–145.

149 K. Bijanzad, A. Tadjarodi, O. Akhavan and M. M. Khiavi, *Res. Chem. Intermed.*, 2016, **42**, 2429–2447.

150 L. W. Lu, M. L. Lv, G. Liu and X. X. Xu, *Appl. Surf. Sci.*, 2017, **391**, 535–541.

151 L. N. Thi, H. Tran Huu, T. N. Ngoc, N. S. M. Viswanath, H. T. T. Le, T. T. T. Phan, L. T. Nguyen, Q. T. H. Ta, H. Le Han, L. N. Tan and V. Vo, *J. Alloys Compd.*, 2023, **960**, 170503.

152 Z. Shen, Q. Han, W. Liu, X. Wang and J. Zhu, *J. Mater. Sci.*, 2019, **54**, 613–624.

153 D. Bokov, A. Turki Jalil, S. Chupradit, W. Suksatan, M. Javed Ansari, I. H. Shewael, G. H. Valiev and E. Kianfar, *Adv. Mater. Sci. Eng.*, 2021, **2021**, 5102014.

154 D. Navas, S. Fuentes, A. Castro-Alvarez and E. Chavez-Angel, *Gels*, 2021, **7**, 275.

155 D. Sánchez-Rodríguez, M. G. Méndez Medrano, H. Remita and V. Escobar-Barrios, *J. Environ. Chem. Eng.*, 2018, **6**, 1601–1612.

156 Y. F. Cui, P. P. Dang, F. H. Wang, P. P. Yuan, W. Liu and Y. P. Pu, *Vacuum*, 2023, **210**, 111899.

157 R. V. William, A. Marikani and P. Thiruramanathan, *J. Mater. Sci.: Mater. Electron.*, 2018, **29**, 10129–10140.

158 T. Xian, H. Yang, J. F. Dai, Z. Q. Wei, J. Y. Ma and W. J. Feng, *Mater. Lett.*, 2011, **65**, 1573–1575.

159 Y. Xi, C. G. Hu, X. M. Zhang, Y. Zhang and Z. L. Wang, *Solid State Commun.*, 2009, **149**, 1894–1896.

160 M. Han, H. Guo, B. Li, J. Jia and W. Wang, *New J. Chem.*, 2017, **41**, 4820–4827.

161 J. Yin, Z. Tan, H. Hong, J. Wu, H. Yuan, Y. Liu, C. Chen, C. Tan, F. Yao, T. Li, Y. Chen, Z. Liu, K. Liu and H. Peng, *Nat. Commun.*, 2018, **9**, 3311.

162 F. Wang, L. Li, W. Huang, L. Li, B. Jin, H. Li and T. Zhai, *Adv. Funct. Mater.*, 2018, **28**, 1802707.

163 J. Li, Z. X. Tang, X. G. Tang, Q. X. Liu and Y. P. Jiang, *FlatChem*, 2021, **28**, 100266.

164 C. Kumari, I. Varun, S. Prakash Tiwari and A. Dixit, *Superlattices Microstruct.*, 2018, **120**, 67–74.

165 R. F. Service, *Science*, 2019, **365**, 108.

166 J. Gao, Q. Huang, Y. Wu, Y. Q. Lan and B. Chen, *Adv. Energy Sustainability Res.*, 2021, **2**, 2100033.

167 Y. M. Xin, C. F. Me and Y. Q. Miu, *Nonferrous Met. Mater. Eng.*, 2020, **41**, 38–45.

168 Y. Jiang, Q. Chen, D. Wang, X. Li, Y. Xu, Z. Xu and G. Guo, *Nano Res.*, 2023, **16**, 6661–6669.

169 Y. Zhang, Y. Chen, R. Liu, X. Wang, H. Liu, Y. Zhu, Q. Qian, Y. Feng, M. Cheng and G. Zhang, *InfoMat*, 2023, **5**, e12375.

170 B. Thomas, C. Tang, M. Ramírez-Hernández and T. Asefa, *ChemPlusChem*, 2023, **88**, e202300104.

171 J. Wang, D. J. Wu, M. H. Li, X. B. Wei, X. M. Yang, M. H. Shao and M. Gu, *Nano Lett.*, 2022, **22**, 5600–5606.

172 L. Ge, Y. Ke and X. Li, *Chem. Commun.*, 2023, **59**, 5795–5806.

173 Q. Guo, C. Zhou, Z. Ma and X. Yang, *Adv. Mater.*, 2019, **31**, 1901997.

174 W. J. Shin, A. H. Granados, H. Hu and M. Tao, *ECS Meeting Abstracts*, 2015, **2**, 790.

175 M. Shi, H. Yang, Z. Zhao, G. Ren and X. Meng, *Chem. Commun.*, 2023, **59**, 4274–4287.

176 X. Jin, L. Ye, H. Xie and G. Chen, *Coord. Chem. Rev.*, 2017, **349**, 84–101.

177 Y. Bai, P. Yang, L. Wang, B. Yang, H. Xie, Y. Zhou and L. Ye, *Chem. Eng. J.*, 2019, **360**, 473–482.

178 K. Wang, L. Zhang, Y. Su, S. Sun, Q. Wang, H. Wang and W. Wang, *Catal. Sci. Technol.*, 2018, **8**, 3115–3122.

179 X. Wang, Y. Wang, M. Gao, J. Shen, X. Pu, Z. Zhang, H. Lin and X. Wang, *Appl. Catal., B*, 2020, **270**, 118876.

180 X. Fan, *Crit. Rev. Environ. Sci. Technol.*, 2022, **52**, 2227–2269.

181 F. Saadati, N. Keramati and M. M. Ghazi, *Crit. Rev. Environ. Sci. Technol.*, 2016, **46**, 757–782.

182 J. Di, J. Xia, M. Ji, S. Yin, H. Li, H. Xu, Q. Zhang and H. Li, *J. Mater. Chem. A*, 2015, **3**, 15108–15118.

183 T. Kanagaraj, P. S. M. Kumar, R. Thomas, R. Kulandaivelu, R. Subramani, R. N. Mohamed, S. Lee, S. W. Chang, W. J. Chung and D. D. Nguyen, *Environ. Res.*, 2022, **205**, 112439.

184 S. Iyyapushpam, S. T. Nishanthi and D. P. Padiyan, International Conference on Advanced Nanomaterials and Emerging Engineering Technologies (ICANMEET), Chennai, India, 2013.

185 J. Zhang, Y. Wang, Y. Wang, X. Shuai, R. Zhao, U. A. Abubakr Yasin, T. Guo, J. Du and J. Li, *Environ. Sci.: Nano*, 2022, **9**, 2979–2989.

186 T. Bavani, J. Madhavan, S. Prasad, M. S. AlSalhi and M. J. AlJaafreh, *Environ. Pollut.*, 2021, **269**, 116067.

187 Z. Long, T. Guo, C. Chen, G. Zhang and J. Zhu, *Front. Microbiol.*, 2023, **14**, 1210790.

188 Y. Wei, Z. Zhang, W. Wang, Z. Song, M. Cai and S. Sun, *ChemPhysChem*, 2023, **24**, e202300216.

189 J. Shang, W. Hao, X. Lv, T. Wang, X. Wang, Y. Du, S. Dou, T. Xie, D. Wang and J. Wang, *ACS Catal.*, 2014, **4**, 954–961.

190 M. Zhu, Z. Sun, M. Fujitsuka and T. Majima, *Angew. Chem., Int. Ed.*, 2018, **57**, 2160–2164.

191 D. Ding, Z. Jiang, D. Ji, M. Nosang Vincent and L. Zan, *Chem. Eng. J.*, 2020, **400**, 125931.

192 Y. Huang, N. Zhang, Z. Wu and X. Xie, *J. Mater. Chem. A*, 2020, **8**, 4978–4995.

193 D. Wu, R. Wang, C. Yang, Y. An, H. Lu, H. Wang, K. Cao, Z. Gao, W. Zhang, F. Xu and K. Jiang, *J. Colloid Interface Sci.*, 2019, **556**, 111–119.

194 Y. Zhang, S. Gu, X. Zhou, K. Gao, K. Sun, D. Wu, J. Xia and X. Wang, *Catal. Sci. Technol.*, 2021, **11**, 4783–4792.

195 C. Xiao, H. Hu, X. Zhang and D. R. MacFarlane, *ACS Sustainable Chem. Eng.*, 2017, **5**, 10858–10863.

196 Q. Wang, J. Du, R. Ouyang, B. Liu, Y. Miao and Y. Li, *Coord. Chem. Rev.*, 2023, **492**, 215281.

197 Y. Li, X. Tan, H. Wang, X. Ji, Z. Fu, K. Zhang, W. Su, J. Zhang and D. Ni, *Nano Res.*, 2023, **16**, 9885–9893.

198 L. Xiao, A. Zhu, Q. Xu, Y. Chen, J. Xu and J. Weng, *ACS Appl. Mater. Interfaces*, 2017, **9**, 6931–6940.

199 M. Wu, J. Yong, H. Zhang, Z. Wang, Z. P. Xu and R. Zhang, *Adv. Healthcare Mater.*, 2023, 2301497.